RADC-TR-89-382
Final Technical Report
March 1990

AD-A223 000

RESONANT COUPLING THROUGH A SLOT TO A LOADED CYLINDRICAL CAVITY - EXPERIMENTAL RESULTS

University of Colorado

John D. Norgard and Ronald M. Sega

APPROVED FOR PUBLIC RELEASE; DISTRIBUTION UNLIMITED.

DTIC
ELECTE
JUN 1 9 1990
S E D

Rome Air Development Center
Air Force Systems Command
Griffiss Air Force Base, NY 13441-5700

90 06 18 212

This report has been reviewed by the RADC Public Affairs Division (PA) and is releasable to the National Technical Information Service (NTIS). At NTIS it will be releasable to the general public, including for ᵢn nations.

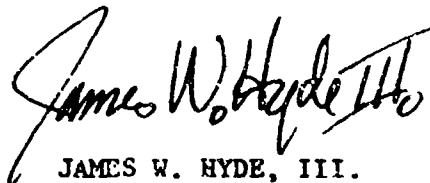RADC-TR-89-382 has been reviewed and is approved for publication.

APPROVED: *[signature]*

CHARLES M. BLANK
Project Engineer

APPROVED: *[signature]*

JOHN J. BART
Technical Director
Directorate of Reliability & Compatibility

APPROVED: *[signature]*

JAMES W. HYDE, III.
Directorate of Plans & Programs

REPORT DOCUMENTATION PAGE

Public reporting burden for this collection of information is estimated to average 1 hour per response, including the time for reviewing instructions, searching existing data sources gathering and maintaining the data needed, and reviewing the collection of information. Send comments regarding this burden estimate or any other aspect of this collection of information, including suggestions for reducing this burden, to Washington Headquarters Services, Directorate for Information Operations and Reports, 1215 Jefferson Davis Highway, Suite 1204, Arlington, VA 22202-4302, and to the Office of Information and Regulatory Affairs, Office of Management and Budget, Washington, DC 20503

1. AGENCY USE ONLY (Leave Blank)	2. REPORT DATE	3. REPORT TYPE AND DATES COVERED
	March 1990	Final Sep 86 to Sep 87

4. TITLE AND SUBTITLE	5. FUNDING NUMBERS
RESONANT COUPLING THROUGH A SLOT TO A LOADED CYLINDRICAL CAVITY - EXPERIMENTAL RESULTS	C - F30602-81-C-0205 PE - 64747F PR - 2064
6. AUTHOR(S) John D. Norgard and Ronald M. Sega	TA - 03 WU - PT

7. PERFORMING ORGANIZATION NAME(S) AND ADDRESS(ES)	8. PERFORMING ORGANIZATION REPORT NUMBER
University of Colorado Department of Electrical Engineering P.O. Box 7150 Colorado Springs CO 80933-7150	N/A

9. SPONSORING/MONITORING AGENCY NAME(S) AND ADDRESS(ES)	10. SPONSORING/MONITORING AGENCY REPORT NUMBER
Rome Air Development Center (RBCT) Griffiss AFB NY 13441-5700	RADC-TR-89-382

11. SUPPLEMENTARY NOTES

RADC Project Engineer: Charles M. Blank/RBCT/(315) 330-2841

12a. DISTRIBUTION/AVAILABILITY STATEMENT	12b. DISTRIBUTION CODE
Approved for public release; distribution unlimited.	

13. ABSTRACT (Maximum 200 words)

The effect of cavity geometry on the energy coupled through a slot aperture is investigated through the use of planar mappings of the internal cavity field. A copper cylinder, closed at both ends, is constructed with copper mesh sections incorporated at the ends of the cylinder and in the cylinder wall opposite a thin slot aperture placed in the wall. The frequencies used for testing are 2-4 GHz.

Internal field mapping is accomplished by placing thin carbon-loaded sheets in the plane of interest and recording the digitized temperature distribution using an infrared scanning system. The sheets are calibrated such that the temperature data is transformed to current densities or electric field strengths.

Using several positions for the detection material, a three-dimensional field profile is obtained. The onset of the internal cavity resonance is studied as it is related to the energy coupled through small apertures.

14. SUBJECT TERMS		15. NUMBER OF PAGES
Electromagnetic Compatibility, (EMC) Electromagnetic Coupling		92
		16. PRICE CODE

17. SECURITY CLASSIFICATION OF REPORT	18. SECURITY CLASSIFICATION OF THIS PAGE	19. SECURITY CLASSIFICATION OF ABSTRACT	20. LIMITATION OF ABSTRACT
UNCLASSIFIED	UNCLASSIFIED	UNCLASSIFIED	UL

NSN 7540-01-280-5500

Standard Form 298 860922
Prescribed by ANSI Std 239.18
298-01

TABLE OF CONTENTS

1.0 INTRODUCTION

This work was performed for the Rome Air Development Center (RADC) under the Po.tdoctoral Program. The Statement of Work for this task and a brief overview of the organization of the report are given below.

1.1 Statement of Work

"Integrated EMS/V techniques and applications." Experimentally and analytically study the phenomenolog·' of electromagnetic (EM) coupling to determine parametrically how EM parameters (frequency, angle of incidence, polarization, power levels, modulation, etc.) and object parameters (number of entry ports; aperture size, shape and orientation; internal cavity size and shape; internal cavity structure, etc.) relate to the measured responses (voltage and current) of electronic components within a cavity. The overall goal is to predict, with confidence, the susceptibility/vulnerability of a complex electronic system while being subjected to intense EM fields.

1.2 Overview

This report has been organized as follows:

First, a brief description of the IR measurement technique that is used to map the interior fields of a cylindrical cavity is presented. Then, the details of the experimental setup for determining the cavity fields are described. This includes a discussion of the development of a wire mesh viewport through which the interior cavity fields can be viewed. Finally, the results of the experimental measurements are presented. Some theoretical predictions are presented firs , followed by the experimental data for several different configurations and frequencies.

-1-

2.0 INTERIOR CAVITY FIELDS

In this report, an infrared (IR) measurement technique is described which can be used to measure electric and/or magnetic fields. This technique is applied to determine the electric fields inside a cavity. The cavity is a long, narrow cylinder of circular cross-section, excited by a long, thin rectangular slot centered in its side. The axis of the slot is parallel to the axis of the cylinder. The slot is illuminated externally by a plane electromagnetic wave polarized along the axis of the cylinder. The two-dimensional electric field is measured in the cross-section of the cylinder. This measurement is repeated at a number of different cross-sections so that a complete three-dimensional map of the electric field is obtained. This measurement procedure is repeated at several frequencies so that the effects of the aperture and the external and internal cylindrical cavity resonances are determined.

This preliminary experimental study of the effects of resonance on the coupling phenomenology was performed to direct the effects of the theoretical study of this problem, which is the subject of another task.

3.0 EXPERIMENTAL TESTS

An overview of the experimental tests that have been designed is given below. Several tests are invisioned and will be performed at RADC and at The University of Colorado at Colorado Springs (CU/Colorado Springs). Explicit details of the test designs are presented later in Section 6.0.

3.1 Experimental Models

A simple model is being constructed at RADC in which classical probe tests will be performed to determine the effects of resonance on coupling phenomenology.

In these tests, a cylinder will be irradiated with a continuous wave (CW) electromagnetic energy over a broad range of frequencies. The angle of polarization between the incident electric field and the axis of the cylinder will be varied. An aperture will be located in the side of the cylinder. The position of the aperture will be varied during the tests. The size, shape and orientation of the aperture will also be varied.

3.2 Test Facilities

The coupling tests will be performed at the Rome Air Development Center (RADC) in the Electromagnetic Compatibility Analysis Facility (EMCAF). Preliminary tests will be performed in the small anechoic chamber; the final tests will be performed in the large anechoic chamber.

All other work needed to develop the test methodologies used at RADC will be performed at CU/Colorado Springs. In particular, a preliminary test of a similar, but simpler, cylinder has been performed in the anechoic chamber (described below in Section 4.0) in the Electromagnetics Laboratory (EML) at CU/Colorado Springs. These preliminary tests used an IR measurement technique to map the fields inside the cylinder.

3.3 Cylinder Designs

The first tests will be performed on a loaded cylinder being fabricated at RADC. This cylinder is being fabricated in modular sections so that its exterior length, interior cavity size, and aperture location, shape, size, and orientation can be easily varied. This cylinder is coaxial with an inner conductor which can be loaded at either end.

The preliminary tests were performed on a similar cylinder fabricated at CU/Colorado Springs. This cylinder is a hollow circular wave guide, constructed with mesh end caps. One interchangeable modular section in the middle of the cylinder can be used to place several different apertures into the side of the cylinder.

4.0 EML ANECHOIC CHAMBER FACILITY

An anechoic chamber was constructed inside the new Engineering and Applied Science Building at CU/Colorado Springs. This chamber is an exact scale model of the Electromagnetic Compatibility Analysis Facility (EMCAF) at the Rome Air Development Center (RADC), at Griffiss AFB, NY. The CU/Colorado Springs chamber is a 0.5625 scale model of the EMCAF chamber. This results in a chamber 28' long by 23' wide by 18' high (interior dimensions), cf. Figure 1. The large absorbers in the specular reflecting areas are 36" long; the short absorbers in the non-specular reflecting areas are 18" long. This produces a quiet zone of approximately 10' x 10' x 5'. The UCCS chamber can be used over a frequency range from approximately 100 MHz to 40 GHz. The chamber wall is of modular paneled construction, minimum performance to meet TEMPEST requirements.

A walk-way to the pedestal area and a walk-way adjacent to the transmitting wall to service the transmitting antennas has been installed inside the chamber. A 4' x 8' shielded equipment and personnel access door to the chamber is located in the transmitting wall.

A source/instrumentation room is located adjacent to the anechoic chamber. This room is 13' long by 17' wide by 10' high (interior dimensions). This room is partitioned into a shielded source room and a shielded instrumentation area. The room has a 3' x 7' shielded personnel access door. Bulkhead feed-through panels have been installed on the centerline of the chamber and at the one-third points along the transmitting wall of the chamber for cable connections to the antennas used to illuminate the systems under test (SUT) inside the anechoic chamber. Four 200W KELTEC amplifiers cover the 1-2 GHz, 2-4 GHz, 4-8 GHz, and 8-18 GHz frequency range. A 10W AR amplifier covers the 0.1-1 GHz frequency range. These amplifiers are driven by an HP 8350B Sweep Oscillator with an HP 83592B RF Plug-In which can operate between 10 MHz to 20.0 GHz, or by an HP 8340A Synthesized Sweeper which can operate between 10 MHz to 26.5 GHz. An HP 8510 network analyzer is used to detect the received signals.

5.0   INFRARED MEASUREMENT TECHNIQUE

The IR measurement technique involves placing a thin, planar, optimized, lossy detection screen in the path of the electromagnetic wave at the position over which the EM field is to be mapped. The details of this technique including the particular requirements on the detection screen, are presented below. This discussion will include the theoretical basis of the technique, the practical realization of the method in the laboratory, and the present capabilities of the experimental system used to implement the technique, both hardware and software, and the accuracy that can be currently achieved by the system developed in the EML laboratory at CU/Colorado Springs.

5.1   IR Theory

The infrared detection technique is based on heating that occurs when electromagnetic energy is absorbed by an object. When the surface temperature rises to 0.1 K or higher above ambient, the induced temperature distribution at the surface (which corresponds to field intensities in that surface) can be detected by an infrared scanning system via emitted thermal radiation. It is possible to relate surface temperature variations to E and H field intensities, since a material can absorb power via E and/or H field coupling. A brief discussion of the mechanism involved in this process is presented below.

5.1.1 EM Absorption

Maxwell's equations describe the relationships between the electric field, E, and the magnetic field, H, as functions of time, space, and the parameters of the material in which the fields reside. The material parameters are conductivity (σ), permittivity (ϵ), and permeability (μ). These parameters can be functions of space and frequency, but no spatial variations are assumed to be present in this study.

Further, this work is being conducted at a single frequency, so the material parameters can be considered constants.

When an EM wave travels through a material, a loss of power can occur due to absorption of the wave.

5.1.2 IR Detection

Absorbed power has been related to field intensities, and can also be shown to relate to induced electric currents J and, in turn, an increase in temperature T in the detection screen.

Thus, energy is absorbed from the incident radiation, the material is heated in the absorbing region, and the localized two-dimensional heating patterns can then be observed using an infrared scanning system.

The IR scanning system used for this work was the AGA Thermovision 780 IR system. The camera is cooled by liquid nitrogen (LN2) and produces a real-time infrared video image of the object being viewed. This image can be displayed on either a color or black and white video monitor. The image is composed of an array of pixels 112 x 128 in size (14,336 pixels).

The image seen by the camera (scanning system) is actually an observation of IR photon flux from a given solid angle from the object. The number of stored digitized levels is 256, but a typical format for display is a color monitor where the range is divided and each level (temperature) is assigned a color. Since infrared emission from a physical object depends not only on the temperature of the body but also on the emissivity ϵ of its surface, different objects at the same temperature will emit different amounts of IR radiation (and, thus, appear to the IR camera to be at different temperatures) if they have different emissivities.

This points out the difficulties which would be encountered in viewing a

complex system of objects/materials -- correlations of actual object temperatures would require knowledge of the emissivities of each surface. For this experiment, the detection screen used was always the same material, oriented normal to the camera; thus, the emissivity remained a constant, and any areas which emitted the same intensity of thermal radiation were, in fact, at the same temperature. This greatly simplified the calibration procedure required for these experiments. The calibration procedure is outlined below in Section 7.0.

5.1.3 Material Optimization

After the electric field absorption problem is solved as a function of screen thickness, conductivity and imaginary permittivity for an incident plane wave, an approximate solution of the thermal problem relating surface temperature to absorbed microwave power can then be obtained. For detection of fields external to the test structure or in cavities, the material is optimized so as to allow only sufficient absorbed power for IR observation, while minimizing the perturbation caused to the field distribution being measured.

For the detection of the electric field scattered from an object, a requirement exists for a material with the properly selected parameters such that sufficient energy is absorbed for a given temperature rise.

Demonstrations of the IR detection of scattered electric fields were accomplished using a screen of carbon paper mounted on styrofoam and placed in the plane of interest. Classic experiments, including Young's Double Slit, Lloyd's mirror, and diffractions from a straight edge, have been studied with good correlation between theory and experiment (cf. Section 5.5). A method of calibrating a material screen for current density and field strength as a function of temperature rise has also been developed (cf. Section 7.2).

5.1.4 Surface Current Detection

An EM wave incident on a metal structure will generally not deposit sufficient energy into the surface to create a direct, detectable temperature increase. Obstacles to direct IR detection of metallic surface currents include high reflectivity with respect to the incident EM wave, low emissivity in the IR, and high thermal conductivity for the diffusion of local heating. The IR detection of the surface current density is accomplished through the interaction of the magnetic field with a thin ferrite-loaded material, placed at the metal surface.

5.1.5 Energy Deposition

For heating to take place in a material, a certain amount of energy must be deposited in the structure. The IR experimental technique is applicable for both continuous (CW) as well as pulsed fields. Electric detection via IR has been seen at 2-4 GHz (CW) [1-14] and at 94 GHz (pulsed) [15,16]. The energy deposited in the illuminated material is the product of power and duration. A steady state condition, with an elevated temperature distribution, will occur as the energy deposited per given time (power) is equal to the energy dissipated, primarily through radiation and convective heat transfer. If the absorbed energy is sufficient in a single EM pulse, the IR technique will provide a rapid means of obtaining the field amplitude distribution.

5.1.6 IR Limitations

The disadvantages of IR detection include limited dynamic range, response time limitations, thermal conduction and convective energy dissipation, and the requirement for sufficient energy deposited in the observed medium. The range for the temperature distribution is a function of the material parameters, available energy, and sensitivity of the detection system. With multiple frame averaging, the discrimination in temperature between pixel elements can be 0.02 K. An observed

temperature rise for a thin resistive material illuminated with less than 40 mW/cm^2 at 3 GHz has exceeded 20 K temperature rise for a range of 30 db. Standard probe measurements, having a greater dynamic range, are made in areas of interest identified initially through IR detection. As thermal mass is increased or encapsulating layers are present at components such as a resistors, the response time to obtain a maximum steady state temperature is increased. Sufficient information as to locations of intense field and current activity can be obtained without achieving a steady-state condition. Caution should be exercised in the analysis of EM energy resulting in heat production as the heat dissipation is accomplished through the thermal mechanisms of conduction and convection as well as radiation in the IR detection range, though calibrations to field can be accomplished.

5.2 Detection Screen

The IR technique is based on Poynting's Theorem for the absorption of electromagnetic energy in a lossy material, when an electromagnetic wave passes through that material. The lossy material forms a detection screen for the absorbed electromagnetic energy. For the special case of a large, but thin, planar screen being irradiated by a plane incident wave, the incident energy is simply related to the absorbed energy through Snell's and Fresnel's Laws. Specifically, the incident electric field intensity is related to the reflected, transmitted, and absorbed electric field intensities by the angles of incidence, reflection, and transmission and the reflection and transmission coefficients.

For a typical detection screen setup, the frequency domain relationships have been developed for a lossy, complex planar screen sandwiched between two other materials, usually air. These relationships have been presented elsewhere [17].

The absorbed EM energy in the detection screen is converted into thermal heat energy. Part of this energy is re-radiated as "black body" energy, which can be

detected with a thermal IR scanning system, e.g., an AGA Thermovision 780 system. For typical carbon based or ferrite detection screens, the radiation is close to a "gray body" and also depends on the emissivity of the surface of the screen. The emissivity of the detection screen used in the experiments reported on later were measured in the EML Laboratory. Some of the absorbed electromagnetic energy which is converted into heat energy is also convected and conducted into the surrounding material, viz., the air around the surface of the screen and the support structure on which the screen is placed.

The conductive heat loss into the supporting structure can be made negligibly small by using a styrofoam base, which has a very small coefficient of thermal conductivity.

The IR measurement technique, therefore, reduces to the simultaneous solution of a non-linear thermal radiation problem from a planar screen, accounting for the convection term, and an electromagnetic boundary value problem of a plane wave incident on a lossy, complex planar screen.

5.3 Thermal Equilibrium

Referring to Figure 2, if the screen has a large cross-sectional area $A = h \times w$ and a small thickness t and lossy, complex constitutive parameters σ, $\epsilon = \epsilon' - j\epsilon''$, $\mu = \mu' - j\mu''$ at the frequency ω, then, in thermal equilibrium [18],

$$P_{abs} = Q_{rad} + Q_{conv} + Q_{cond}$$

where

$$P_{abs} = \int_V (\sigma E^2 + \omega \epsilon'' E^2 + \omega \mu'' H^2)\,dV$$

and

$$Q_{rad} = \kappa \, \epsilon_t (T^4 - T_0^4)$$

$$Q_{conv} = \frac{1.57 \, (T-T_0)^{1.25}}{h^{0.25}}$$

$$Q_{cond} = 0$$

The volume integral is over the detection screen. κ is the Stefan-Boltzmann constant, ϵ_t is the emissivity of the screen at the angle of radiation to the IR camera. T is the local elevated temperature of the screen (a function a position over the screen) and T_0 is the ambient background temperature. These tests are usually performed in the EML anechoic chamber for precise control of the background environment.

The IR camera, after calibration against a known black body reference source, measures the temperature $T(x,y)$ over the surface of the detector screen. Since the detection screen is purposely made very thin, the temperature distribution normal to the surface of the screen is assumed to be isothermal. The absorbed electric field intensity, which is assumed to be constant through the screen thickness (normal to the surface of the screen), can be determined by the simultaneous solution of the above thermal and electromagnetic problems.

Using Snell's and Fresnel's Laws, the incident electric (or magnetic) field intensity can then be determined from a solution of the electromagnetic boundary value problem at the surface of a planar interface between air and the lossy, complex detection screen.

Since the detection screen is thin (usually < 100 μ m), it will not significantly perturb the incident field to be measured. Also, the constitutive parameters of the screen (σ, ϵ'', μ'') are adjusted so that only a small fraction of the incident power is intercepted by the screen (usually P_{abs} < 0.05 P_{inc}).

A further simplification can be realized if a carbon type screen is used. For this material, $\omega\epsilon'' << \sigma$ and $\omega\mu'' << \sigma$, and the volume integral over the detection screen for the absorbed power reduces to a integral over the square of the electric field intensity. Similarly, if a ferrite type screen is used on the surface of a metal to detect the surface current through the magnetic field, the volume

integral reduces to an integral over the square of the magnetic field intensity, since the tangential electric field is zero. The detector screen, therefore, can be optimized to minimally perturb the incident field and to detect either the electric or the magnetic field intensity.

The net result is a two-dimensional image of the thermal pattern on the detection screen which is directly correlated to the incident electric or magnetic field intensity in the plane of the screen.

5.4 IR System Capabilities

An AGA Thermovision 780 system is used to measure the local surface temperature of the detection screen as a function of position over the screen and as a function of time in a pulsed mode of operation. The hardware and software capabilities of this system are described below.

5.4.1 IR System Hardware Capabilities

The present system has two IR detectors: a short wave detector between 2 to $6 \mu m$; a long wave detector between 8 to 14 μm. Wide angle $(20.0°)$, regular $(7.0°)$, and telephoto $(3.5°)$ IR lens are available to frame the detection screen on the detectors at various stand-off distances for various screen sizes. Several IR mirrors are also available for use, if required. Each two-dimensional frame of the digitized IR image on the detection screen is composed of 128 x 128 pixels. Each pixel is represented by an 8-bit word, which allows for 256 levels of contrast. The detectors are capable of resolving a 0.1 K change in temperature from pixel to pixel. With multiple frame averaging, a 0.02 K change can be detected. As an example, without averaging, the threshold sensitivity is approximately 0.1 mW/cm^2 inciden power, if the detector screen is 80 μm in thickness and composed of carbon paper with a conductivity of 8 mhos/m. A two-dimensional digitized image of the thermal pattern on the detection screen can be viewed on a black and white or color monitor or stored in the memory of the system for later viewing and/or processing.

5.4.2 IR System Software Capabilities

The regular IR camera interface with its local digitizer has been modified to interface with an IBM AT/PC [19,20]. Each sample takes 4.9 μs to detect and digitize. Each complete frame takes, therefore, approximately 89 ms to process. At the rate of 205 K samples per second, 15 frames can be taken in approximately 2.5 seconds. This is the present limit of the memory storage of the system. This technique has been applied to CW and pulsed waves in the RF, microwave, and mm wave regions.

5.5 IR Accuracy

To determine the accuracy of the IR measurement technique, two simple microwave interference experiments were performed. These tests were the measurement of the far-field interference from a virtual (image) source through a ground plane (Lloyd's Mirror) and the measurement of the near field (Fresnel Zone) diffraction from an edge. These experiments were chosen because theoretical solutions for the interference patterns are known [21,22].

5.5.1 Scattering from a Planar Surface (Lloyd's Mirror)

The experimental setup in the EML anechoic chamber is shown in Figure 3a. A large planar ground plane is placed near a horn antenna, operating at L band (1-2 GHz). Due to the high conductivity of the metal of the ground plane, induced surface charges and currents are excited on the surface of the plane. These induced charges and currents launch a scattered wave from the surface of the plate. This scattered wave can be modeled simply as a virtual (image) antenna radiating in the absence of the ground plane. If a large carbon detection screen is placed near the ground plane, as shown in Figure 3a, the interference pattern between the horn and its image can be measured. Referring to Figure 3b, the intensity of the interference pattern, as a function of position across the detection screen measured from the center line of the screen (point of intersection of the mirror with the screen), is

shown dotted, as calculated from EM theory, and as a solid line, as measured with the IR technique. The agreement is particularly good at all points except the minima. The small errors at the minima are, most likely, due to thermal diffusion from the hotter areas surrounding the cool spot at each minimum.

5.5.2 Diffraction from an Edge

The experimental setup in the EML anechoic chamber is shown in Figure 4a. In a similar experiment to the one described above, a large conducting plane is placed on edge near a horn antenna, operating at L band (1-2 GHz). Due to the diffraction effects at the knife edge of the plane, a scattered wave from the induced line source of current on the edge of the plane will interfere with the direct wave from the source antenna. If a carbon detection screen is placed near the ground plane, as shown in Figure 4a, the interference pattern can be measured in the near field of the diffraction source. Referring to Figure 4b, the intensity of the interference pattern, as a function of position across the detection screen measured from the center line of the screen (point of projection of the edge of the ground plane to the screen), is shown dotted, as calculated from EM theory, and as a solid line, as measured with the IR technique. Again, the agreement between theory and measurement is quite good.

6.0 CYLINDRICAL MODELS (DETAILS)

A simple cylindrical model is being constructed at RADC on which classical probe tests will be performed to determine the effects of resonance on coupling phenomenology. These tests will be performed in the EMCAF Anechoic Chamber at RADC.

6.1 Cylinder Design

The cylinder is approximately 1 meter in length and 3" inside diameter. The cylinder is loaded with an inner coaxial line which is terminated to the end caps of the cylinder through load impedances.

An aperture is located in the wall of the cylinder. The cylinder is constructed in a modular way so that the aperture can be positioned at any angle around the circumference of the cylinder and can be located at various discrete positions along the length of the cylinder. The aperture is also designed in a modular fashion. Different apertures can be introduced into the side of the cylinder by replacing a section of a removable plate in the side of the cylinder. In this manner, the size and shape of the aperture can easily be changed. Also, the orientation of the axis of the aperture can be changed relative to the axis of the cylinder.

The overall length of the cylinder and the internal cavity size can be adjusted by adding shorting bulkheads inside the cavity or by adding dummy sections to the outside of the cylinder.

The last section of the cylinder interior contains an isolated section designed to contain a fiber optics telemetry system. This system will be designed to transmit the detected voltage on the inner conductor of the coax to a receiver in the instrumentation room in the EMCAF facility.

7.0 IR SYSTEM CALIBRATION

For each detection screen material, the IR system must be calibrated, as discussed below.

7.1 Isothermal Units to Temperature

The IR camera system provides data in the form of "ISU" or "isotherm" units. For observations of targets with surface temperatures which cover a wide range of values, correlation from ISU values to temperature requires complicated calculations and very detailed equipment calibration [2,19]. For this application, however, the laboratory ambient temperature range is approximately between 290 and 310 K, and the temperature increase of the detection screen is on the order of 5 K or less. Thus, a linear relationship is assumed between the ISU units and temperature when examined as differential quantities (that is, for two objects, the difference between ISU values corresponds in an approximately linear fashion to the difference between their temperatures).

$$\Delta T = K * (\Delta \text{ ISU})$$

where

$$K = \text{Thermal Range}/256$$

Although correlation to absolute temperature measurements is more complicated, the above equation provides a method for transforming from a difference between two ISU values to a temperature difference between two points.

7.2 Relative Temperature Differences Correlated to Electric Fields

For electric field detection, a carbon screen is used. A method to quantify the increase in temperature in the carbon screen which results from irradiation with EM energy has been described above. The next step is to relate the temperature increase to the magnitude of the electric field at each point in the carbon screen.

To develop a mathematical model for temperature increase as a function of electric field, the heating that occurs is treated as a resistive power loss, familiar from circuit theory. That is, the power dissipated by a volume carrying an electric current is $P = I^2R$, where I is the total current and R is the total resistance of the volume. For the case of electric currents in the carbon detection screen, the current per unit area (the current density, J) is related to the total resistance of the material, which is related to the conductivity of the material.

For a material with uniform conductivity of width W, length L and thickness t, the total current will be

$$I = \int J dA$$

where A = cross sectional area of the material. J is assumed to be uniform for small regions of the carbon detection screen (corresponding to the area viewed by a single pixel of the IR scanning system). The resistance of this volume is [23]

$$R = L/A \ \sigma = L/Lt \ \sigma = 1/t \ \sigma$$

Thus, the power absorbed per unit area is

$$\frac{\text{Power absorbed}}{\text{Unit area}} = J^2R = \frac{J^2}{t\sigma}$$

To determine J, it is assumed that the power absorbed per unit area over a given time produces heat, resulting in a temperature increase which is approximately a linear function of power absorbed, and, in turn, is proportional to the square of the current density present [2,17]. This implies that the increase in temperature can be modeled as

$$\Delta T = aJ^2 \quad (a = \text{proportionality constant})$$

To account for imperfect agreement with such an idealized model, however, a linear correction term is included in the relation discussed above. Thus

$$\Delta T = aJ^2 + bJ$$

or

$$aJ^2 + bJ - \Delta T = 0$$

So, using the quadratic equation,

$$J = \frac{-b + (b^2 + 4a \; \Delta T)^{\frac{1}{2}}}{2a}$$

Note here that "a" must be positive, as is T; therefore, the term under the radical is always positive and greater than b^2. (that is, the radical term is always > b). The positive sign is used only to insure that J (current density) is never negative.

Determination of the constants "a" and "b" is fairly straightforward. A known current is passed through the carbon screen and the resultant heating which occurs is recorded (in terms of ISU units, which then provides a measurement of temperature increase). The data points obtained with this method are then used to determine the values of "a" and "b" in the equation above. It should be noted that the equation is constrained to intersect the point (0,0), based on the logical assumption that zero electric current would result in zero temperature increase.

Empirically determined values of "a" and "b" for the carbon paint (as well as two other detection screens commonly used in the CU/EML Lab, carbon paper and a carbon loaded "space" cloth) are shown in Table I.

7.3 Experimental Arrangement

The experimental arrangement for performing this current-to-temperature correlation is shown in Figure 5. In the case of the carbon paint on artboard or carbon paper, the test screen used is the same as the detection screen used for the experimental data taken for this report. The screen was prepared for this correlation by placing two parallel copper tape strips on the surface (to be used as electrodes). Silver paint was applied on the copper and carbon paint surfaces overlapping the junction to ensure that good electrical contact was made. With an identical piece of the carbon screen next to the test screen (to serve as a reference at ambient temperature) the current through the test screen was incrementally

increased while the differential temperature levels between the test and reference screens were recorded by the Thermovision system. It was assumed that the current density was uniformly distributed throughout the carbon paint.

With the values of a and b known, the final correlation from current density to electric field magnitude can be made by noting that (from Maxell's form of Ohm's Law)

$$J = \sigma E$$

Thus, solving for the magnitude of the E field by combining the above equations

$$E = \frac{1}{\sigma} \frac{(-b + [\, b^2 + 4a(K \cdot \Delta ISU)\,]^{\frac{1}{2}})}{2a}$$

Now note that an expression has been provided to relate electric field magnitude to observed thermal heating. To arrive at the magnitude of the E field incident at the surface of the carbon screen, however, some additional corrections must be applied to the above equation.

7.3.1 Corrections 1

The electric field magnitude given by the above equation is that portion of the incident electric field absorbed by the carbon screen -- that is, the percentage which is i) not reflected at the surface and, ii) the percentage which is then absorbed rather than passing through the material. The percentage of the incident electric field which is reflected, absorbed, and transmitted by the carbon screen is now considered.

It can be shown that the power absorbed by a conductive film is related to the magnitude of the incident electric field by Snell's and Fresnel's Laws [23].

Note that the physical parameters of the material, viz. thickness (t), conductivity (σ), permeability (μ), and permittivity (ϵ), must be known.

Thus, for the carbon paint screen, with an average thickness on the order of 80 microns, 5% of the incident power is absorbed. Since power is related to the square of the electric field, this gives an incident electric field intensity of approximately 2%.

To correct for reflection and transmission of part of the incident EM radiation, the above equation is also divided by the percentage attributed to actual absorption to give:

$$E_{inc} = E_{abs} \ 100/\ 2$$

7.3.2 Corrections 2

Secondly, the correlation method outlined above relates the increase in screen temperature to the magnitude of a constant electric current applied to the screen; but, the experimental data recorded by the IR camera system is the heating which occurs due to currents induced by an electric field which is a function of both time and space.

To address the issue of spatial variations of the electric field, note that the screen is on the order of 80 microns thick, thus, the variation of the electric field magnitude through the carbon screen (at any instant) is negligible.

With respect to the time varying nature of the EM wave, note that the energy absorbed by the carbon screen is a function of the EM power present inside the screen, which is taken as proportional to the square of the RMS value of the (E or H) field. Thus the magnitude of the E field calculated above is the RMS value of the incident E field and must be multiplied by $\sqrt{2}$ to yield the results desired, the peak value for the E field incident on the carbon screen.

8.0   EXPERIMENTAL SETUP

The particular geometry and details of the experimental setup to measure the interior fields of a cavity excited through a small thin slot aperture are described below.   The parameters of the RF source are also given.   For this measurement, a thin carbon disk placed inside the cavity was used as a detector.   A special double shielded wire mesh end cap was fabricated to replace the solid end cap of the cylinder so that the carbon disk detector could be viewed.   Salient details of the detector and viewport are also discussed.

8.1   Cavity/Aperture Geometry

A one meter length of copper pipe, with a 4" inside diameter, was placed horizontally in the EML anechoic chamber on a block of styrofoam, as shown in Figure 6.   A 3" long rectangular slot was cut into the side of the cylinder half way between the ends of the cylinder, with the long axis of the slot parallel to the axis of the cylinder.   The width of the slot was 25 thousandths of an inch.   Tnis slot size was chosen to model a long thin seam or crack.   A circular section of carbon paper of thickness 80 μm and conductivity 8 mhos/m was placed on a round plug of art board and placed inside the cylinder.   The art board was used to stiffen the carbon paper and to keep it flat and to position the disk inside the cylinder.   The carbon paper was trimmed off the outer edge of the disk so as not to touch the metal pipe and to short out the induced charges or currents on the carbon paper.   This disk was moved back and forth inside the cylinder to detect the circular cylinder electric fields inside the cavity at any cross-section of interest.

One end of the cylinder was fitted with a solid copper end cap.   The other end of the cylinder, which served as a viewport for the IR radiation, was fitted with a double layer of copper wire mesh, which was bonded to the end of the cylinder.

This wire mesh end cap acts like a solid shield at the microwave frequencies (1 - 18 GHz) of this experiment. While the wire mesh appears to be opaque to energy at the microwave wavelengths, it is still transparent to the energy at the IR wavelengths, which are approximately 10,000 times shorter in length. The mesh size used was approximately 1/16" opening.

8.2   RF Source Parameters

A vertically polarized horn antenna, operating in the 1 - 18 GHz range, was used to illuminate the closed end-cap cylinder. The aperture was aligned on the bore sight of the horn pattern to produce maximum coupling. The frequency of the source was varied to produce a range of effects. Specifically, the cavity wave guide mode was excited below and above cut-off. Also, the frequency was swept across several of the circular cylinder cavity resonant frequencies and the aperture resonant frequency.

9.0 IR RESULTS

The measured IR results are presented below for the two cases of on and off the resonant frequency of the aperture. Other cases will be presented in another report.

The measured results are presented as thermograms of the raw, unprocessed data. Processed relief maps and contour plots of the cross-sectional data are also presented. Several longitudinal slices along the center line of the cylinder are also produced.

9.1 Theoretical Predictions

Before the experimental results are given, however, several expected theoretical results are presented. This includes the electric and magnetic fields produced in the aperture, the circular cylinder wave guide modes that can be excited inside the cavity, and the resonant frequency of the aperture and cavity modes.

9.1.1 Aperture Coupling

As shown in Figure 7, for a good conductor, the electric field intensity E becomes normal to the surface of the conductor as it approaches the surface of the conductor, since the electromagnetic boundary conditions require that the tangential component of the electric field vanish at the surface of the conductor. When a small aperture is cut into the side of the metal, the electric field will penetrate through the hole into the cavity formed behind the conductor. Strong normal fields will exist inside the aperture and will fringe inside the cavity and terminate normally on the inside surface of the conductor. This aperture coupled field can be well approximated by a small normal electric dipole moment $\bar{p}$ situated inside the aperture. The electric field of the coupled aperture excitation should look similar to the electric field of a dipole over a ground plane, i.e., 1 ∴ a monopole inside the cavity.

If a carbon disk is used as a detection screen, the IR thermograms will show the isothermal patterns on the disk; these isotherms correspond roughly to the contours of constant electric field strength. These curves are the family of equi-contours orthogonal to the solid lines shown in Figure 7c. These equi-contours are shown as dotted lines in Figure 7c. Although Figure 7 is shown for a plane, similar results are expected for a circular cylinder at the frequencies tested.

Similarly, as shown in Figure 8, the magnetic field intensity H becomes tangent to the surface of the conductor as it approaches the surface of the conductor, since the electromagnetic boundary conditions require that the normal component of the magnetic field vanish at the surface of the conductor. When a small aperture is cut into the side of the metal, the magnetic field will penetrate through the hole into the cavity formed behind the conductor. Strong normal fields will exist inside the aperture and will fringe inside the cavity and return to the outside of the aperture (magnetic flux lines do not terminate on the side of the conductor). The magnetic field lines that pass close by the inside surface of the conductor will be tangent to the surface of the conductor. This aperture coupled field can be well approximated by a small tangental magnetic dipole moment $\bar{m}$ situated inside the aperture. The magnetic field should look similar to the magnetic field of a magnetic dipole over a ground plane, i.e., like a monopole inside the cavity.

If a ferrite disk is used as the detection screen, the IR thermograms will show the isothermal patterns on the disk; these isotherms correspond roughly to the contours of constant magnetic field strength. These curves are the family of equi-contours orthogonal to the solid lines shown in Figure 8c. These equi-contours are shown as dotted lines in Figure 8c.

9.1.2 Circular Cylinder Waveguide Modes

The dominant mode in a circular waveguide is the TE_{11} mode. Higher order TE and TM modes can also be excited by the dipole like fields which penetrate through the aperture.

A two-dimensional contour plot of the first few waveguide modes that are likely to be excited are shown in Figure 9.

9.1.3 Resonant Frequencies

The resonant frequency of a 3" by 25 thousands rectangular slot is approximately 1.97 GHz. This is the frequency whose corresponding free space wavelength makes the circumference of the slot a full wavelength. For a thin slot, the length of the slot is approximately a half wavelength.

The resonant frequency of the TE and TM circular cylindrical cavity modes can be calculated using the expressions [23]

$$f_{r_{mnp}}^{TM} = \frac{c}{2\pi} \sqrt{(\frac{r_{mn}}{\rho_0})^2 + (\frac{p\pi}{z_0})^2}$$

or

$$f_{r_{mnp}}^{TE} = \frac{c}{2\pi} \sqrt{(\frac{r'_{mn}}{\rho_0})^2 + (\frac{p\pi}{z_0})^2}$$

where m,n are the model indices in the transverse cross-section of the cylinder of radius ρ_0 and p is the modal index in the longitudinal direction of a cylinder of length z_0. In the above expressions, r and r' are the nth roots of the Bessel Function (of the first kind) and its derivative of order m, respectively, i.e.,

$$J_m(r_{mn}) = 0 \qquad n = 1, 2, 3, \ldots$$

$$J'_m(r'_{mn}) = 0 \qquad n = 1, 2, 3, \ldots$$

The roots of the lowest order TE and TM modes are given in Table II.

For the cylinder used in these tests with a radius $\rho_0 = 2"$ and a length $z_0 = 1m$, the resonant frequencies of the first few modes are:

$$f^{TE}_{r111} = 1.73 \text{ GHz}$$

$$f^{TM}_{r010} = 2.25 \text{ GHz}$$

$$f^{TE}_{r211} = 2.86 \text{ GHz}$$

9.2 IR Measured Results

Two series of tests were performed: one at a frequency of 1.75 GHz, which is just above the lowest order circular cavity mode; and one at 1.97 GHz, which is at the resonant frequency of the aperture. The 1.75 GHz tests are, therefore, below the resonant frequency of the aperture, but above the cutoff of the cavity mode.

In all of the cross-sectional thermograms to be presented in this section, the measured IR results are presented as relief maps or as isothermal equi-contour plots, cf. Figure 10 or 12.

In all of the figures shown in relief, the measured IR intensities at each pixel location on the cross-section of the carbon detection disk are mapped in relief over the corresponding vertical or horizontal position on the disk (measured in terms of pixel number). The raw data on the disks from the IR measurements are found inside a 4" diameter circle centered inside the rectangular relief map shown for each case. The digitized format for a frame from the IR camera is square. All of the data shown outside the 4" diameter circle is background noise seen by the camera outside the circular cross-section of the cylinder. This noise is essentially the anechoic walls of the chamber behind the cylinder, but in the view of the edges of the camera's lens. The relief maps are rotated such that the position of the aperture is located on the left side of the figures. In all cases, data were taken at each 0.5 cm position throughout the length of the aperture, however, after passing the edge of the aperture, data were taken at larger spacings.

9.2.1 1.75 GHz IR Test Results (Non-resonant Case)

Figures 10a-n show, in relief, the measured IR results at 1.75 GHz on

the circular carbon detection screen at a number of different cross-sections inside the circular cavity. Each cross-section is labeled on the top of the relief map with the number of centimeters it is away from the center of the aperture. At this frequency, the aperture is non-resonant.

Figures 10a-n also show equi-contour (isothermal) plots of the same data.

Figure 11 presents a relief map of a longitudinal slice of the data through the center of the cylindrical cavity. This map was generated as a composite of horizontal slices through the cross-sectional thermograms presented in Figures 10a-n.

A study of Figures 10 and 11 reveals a non-resonant "cool" electric dipole field in the immediate vicinity of the aperture (cf. Figure 10a) coupling slowly into a pure waveguide/cavity mode at the ends of the circular cylindrical cavity. Since the aperture is not resonant, the cavity fields decay (evanescent modes) with distance from the aperture.

9.2.2 1.97 GHz IR Test Results (Resonant Case)

Figures 12a-p show, in relief, the measured IR results at 1.965 GHz on the circular carbon detection screen at a number of different cross-sections inside the circular cavity. Each cross-section is labeled on the top of the relief maps with the number of centimeters it is away from the center of the aperture. At this frequency, the aperture is resonant.

Figures 12a-p also show equi-contour (isothermal) plots of the same data.

Figure 13 presents a relief map of a longitudinal slice of the data through the center of the cylindrical cavity. This map was generated as a composite of horizontal slices through the cross-sectional thermograms presented in Figures 12a-p.

A study of Figures 12 and 13 reveals a resonant "hot" electric dipole field throughout the region of the aperture (cf. Figure 12a) coupling strongly into a pure waveguide/cavity mode at the ends of the circular cylindrical cavity. Since the aperture is resonant, the cavity fields do not decay significantly with distance from the aperture.

10.0 CONCLUSIONS

A comparison of the IR results presented for resonant and non-resonant coupling through a thin slot to a circular cylindrical cavity shows the strong influence on the coupled field intensity that can occur when the aperture is "tuned" to receive the incident energy.

If the coupling is directed to a pick-up wire toward the ends of the cavity, very little energy would be received by that wire for the non-resonant aperture case; however, a large amount of energy would be received by that wire for the resonant aperture case. For the resonant aperture case, the wire could be positioned anywhere in the cavity and it would be situated in an area of large electric field energy density. The position of the pick-up wire is much more critical for the non-resonant aperture case.

It is concluded that frequency and position are important parameters to consider when studying the intensity of the energy coupled through an aperture and the resultant electromagnetic interference (EMI) with a pick-up wire located inside the cavity.

Further studies will be conducted with different aperture shapes, sizes, orientations and locations on the cylinder at different frequencies relative to the resonant frequencies (and their harmonics) of the aperture and the internal cavity modes.

Further work will be done to add a wire to the inside of the cavity and to adjust the internal cavity resonant frequency relative to the aperture resonant frequency. Also, the external size of the cylinder will be adjusted independently of the internal cavity size to study the effect of the external resonance frequency of the cylinder on the overall coupling phenomenology.

11.0 PUBLICATIONS

The following is a list of the publications produced under this contract.

Journal Articles

1. R. M. Sega and J. D. Norgard, "An Infrared Measurement Technique for the Assessment of Electromagnetic Coupling," IEEE - NS Transactions, Vol. 32, No. 6, December 1985, pp. 4330-4332.

2. R. M. Sega and J. D. Norgard, "Infrared Measurement of Scattering and Electromagnetic Penetrations through Apertures," IEEE - NS Transactions, Vol. NS-33, No. 6, pp. 1658-1663, December 1986.

Conference Proceedings

1. R. M. Sega and J. D. Norgard, "An Infrared Measurement Technique for the Assessment of Electromagnetic Coupling," Proceedings of the Nuclear and Space Radiation Effects Conference, Monterey, CA, July 1985.

2. R. M. Sega and J. D. Norgard, "Infrared Detection of Microwave Scattering from Cylindrical Structures," Proceedings of the 1986 URSI Winter Meeting, Boulder, CO, January 1986.

3. D. W. Metzger, R. M. Sega, J. D. Norgard and P. Bussey, "Experimental and Theoretical Techniques for Determining Coupling Through Apertures in Cylinders," 1986 Nuclear Electromagnetic Meeting, Albuquerque, NM, May 1986.

4. J. D. Norgard and R. M. Sega, "Infrared Measurement of Scattering and Electromagnetic Penetrations through Apertures," Nuclear and Space Radiation Effects Conference, Providence, RI, July 1986.

5. J. D. Norgard and R. M. Sega, "Three-Dimensional Determination of Cavity Resonance and Internal Coupling," Proceedings of the 1987 URSI Winter Meeting, Boulder, CO, January 1987.

6. J. D. Norgard and R. M. Sega, "Microwave Fields Determined from Thermal Patterns," SPIE Symposium, Orlando, FL, May 1987.

7. D. Fredal, P. Bussey, R. M. Sega and J. D. Norgard, "Hardware and Software Advancement for Infrared Detection of Microwave Fields," SPIE Symposium, Orlando, FL, May 1987.

REFERENCES

1. R. M. Sega, V. M. Martin, D. Warmuth and R. W. Burton, "An Infrared Application to the Detection of Induced Surface Currents," Modern Utilization of Infrared Technology VII, Vol. 304, SPIE (The International Society for Optical Engineering), pp. 84-91, August 1981.

2. R. M. Sega, "Infrared Detection of Surface Currents on Flat Plates," RADC TR 82-308, 1982.

3. R. M. Sega and G. J. Genello, "Infrared Thermography Techniques for EMI/EMC Measurements," Proceedings of Electromagnetic Compatibility '83, Arlington, VA, pp. 29-33, August 1983.

4. Gary D. Wetlaufer, Ronald M. Sega and John D. Norgard, "Optimizing Thin Magnetic Material for the Thermographic Detection of Microwave Induced Surface Currents," Proceedings of the 1985 APS/URSI Symposium, Vancouver, British Columbia, Canada.

5. R. M. Sega and J. D. Norgard, "An Infrared Measurement Technique for the Assessment of Electromagnetic Coupling," Proceedings of the Nuclear and Space Radiation Effects Conference, Monterey, CA, July 1985, and IEEE - NS Transactions, Vol. 32, No. 6, pp. 4330-4332, December 1985.

6. R. M. Sega and J. D. Norgard, "Infrared Detection of Microwave Scattering from Cylindrical Structures," Proceedings of the 1986 URSI Winter Meeting, Boulder, CO, January 1986.

7. D. W. Metzger, R. M. Sega, J. D. Norgard and P. Bussey, "Experimental and Theoretical Techniques for Determing Coupling Through Apertures in Cylinders," 1986 Nuclear Electromagnetic Meeting, Albuquerque, NM, May 1986.

8. J. D. Norgard and R. M. Sega, "Infrared Measurement of Scattering and Electromagnetic Penetrations Through Apertures," Nuclear and Space Radiation Effects Conference, Providence, RI, July 1986, and IEEE - NS Transactions, Vol. NS-33, No. 6, pp. 1658-1663, December 1986.

9. R. M. Sega and J. D. Norgard, "Infrared Diagnostic Techniques for High-Power Microwave Measurements," Proceedings of High Power Microwave Technology Meeting, (AFWL), Albuquerque, NM, December 1986.

10. J. D. Norgard and R. M. Sega, "Three-Dimensional Determination of Cavity Resonance and Internal Coupling," Proceedings of the 1987 URSI Winter Meeting, Boulder, CO, January 1987.

11. J. D. Norgard and R. M. Sega, "Microwave Fields Determined From Thermal Patterns," Proceedings of the 1987 SPIE Symposium, Orlando, FL, May 1987.

12. R. M. Sega, D. Fredal and J. D. Norgard, "Initial Feasibility Test of an Infrared Diagnostic for High Power Microwave Application," Proceedings of the 1987 SPIE Symposium, Orlando, FL, May 1987.

13. J. D. Norgard and R. M. Sega, "Measured Internal Coupled Electromagnetic Fields Related to Cavity and Aperture Resonance," Proceedings of the 1987 NSRE Conference, Snowmass, CO, July 1987.

14. R. M. Sega and J. D. Norgard, "Expansion of an IR Detection Technique Using Conductive Mesh in Microwave Shielding Applications," Proceedings of the 1987 SPIE Symposium, San Diego, CA, August 1987.

15. Ronald M. Sega, Cody A. Benkelman and John D. Norgard, "Measurement of Antenna Patterns at 94 GHz Using Infrared Detection," Transactions of SPIE, Washington, D.C., June 1985.

16. C. Benkelman, J. D. Norgard and R. M. Sega, "Infrared Detection of Millimeter Wave Antenna Patterns," Proceedings of the Millimeter Wave/Microwave Measurements and Standards Meeting, Huntsville, AL, November 1986.

17. G. D. Wetlaufer, M.S. Thesis, University of Colorado, 1985.

18. R. Seigel and J. R. Howell, Thermal Radiation Heat Transfer, 2nd ed., McGraw-Hill Book Company: New York, 1981.

19. [82085-1] AGA Thermovision 780 Operating Manual, 1980, by AGA Systems AB.

20. D. Fredal, P. Bussey, R. M. Sega and J. D. Norgard, "Hardware and Software Advancement for Infrared Detection of Microwave Fields," Proceedings of the 1987 SPIE Symposium, Orlando, FL, May 1987.

21. Paul Lorrain and Dale R. Corson, Electromagnetic Fields and Waves, 2nd ed., W. H. Freeman and Company: New York, 1970.

22. E. C. Jordan and K. D. Balmain, Electromagnetic Waves and Radiating Systems, 3rd ed., Prentice-Hall, Inc.: Englewood Cliffs, NJ, 1982.

23. J. D. Kraus and K. R. Carver, Electromagnetics, 2nd ed., McGraw-Hill Book Company: New York, 1973.

Table I. Values of a & b

	Carbon Paint	Carbon Paper	Space Cloth
"a"	41.81	4.241	7.507
"b"	-.6533	-.4755	.7658

Table II. Roots of the Bessel Function and its Derivative
(From: Marcuvitz, Waveguide Handbook)

—Roots of $J_m(x) = 0$

$$x_{mn} = \left(m + 2n - \frac{1}{2}\right)\frac{\pi}{2} - \frac{4m^2 - 1}{4\pi(m + 2n - \frac{1}{2})} - \frac{(4m^2 - 1)(28m^2 - 31)}{48\pi^2(m + 2n - \frac{1}{2})^3} \cdots$$

n \ m	0	1	2	3	4	5	6	7
1	2.405	3.832	5.136	6.380	7.588	8.771	9.936	11.086
2	5.520	7.016	8.417	9.761	11.065	12.339	13.589	14.821
3	8.654	10.173	11.620	13.015	14.372			
4	11.792	13.323	14.796					

—Roots of $J'_m(x') = 0$

$$x'_{mn} = \left(m + 2n - \frac{3}{2}\right)\frac{\pi}{2} - \frac{4m^2 + 3}{4\pi(m + 2n - 1)} - \frac{112m^4 + 328m^2 - 9}{48\pi^2(m + 2n - 1)^3} \cdots, \quad m > 0$$

n \ m	0	1	2	3	4	5	6	7
1	3.832	1.841	3.054	4.201	5.317	6.416	7.501	8.578
2	7.016	5.331	6.706	8.015	9.282	10.520	11.735	12.032
3	10.173	8.536	9.969	11.346	12.682	13.987		
4	13.324	11.706	13.170					
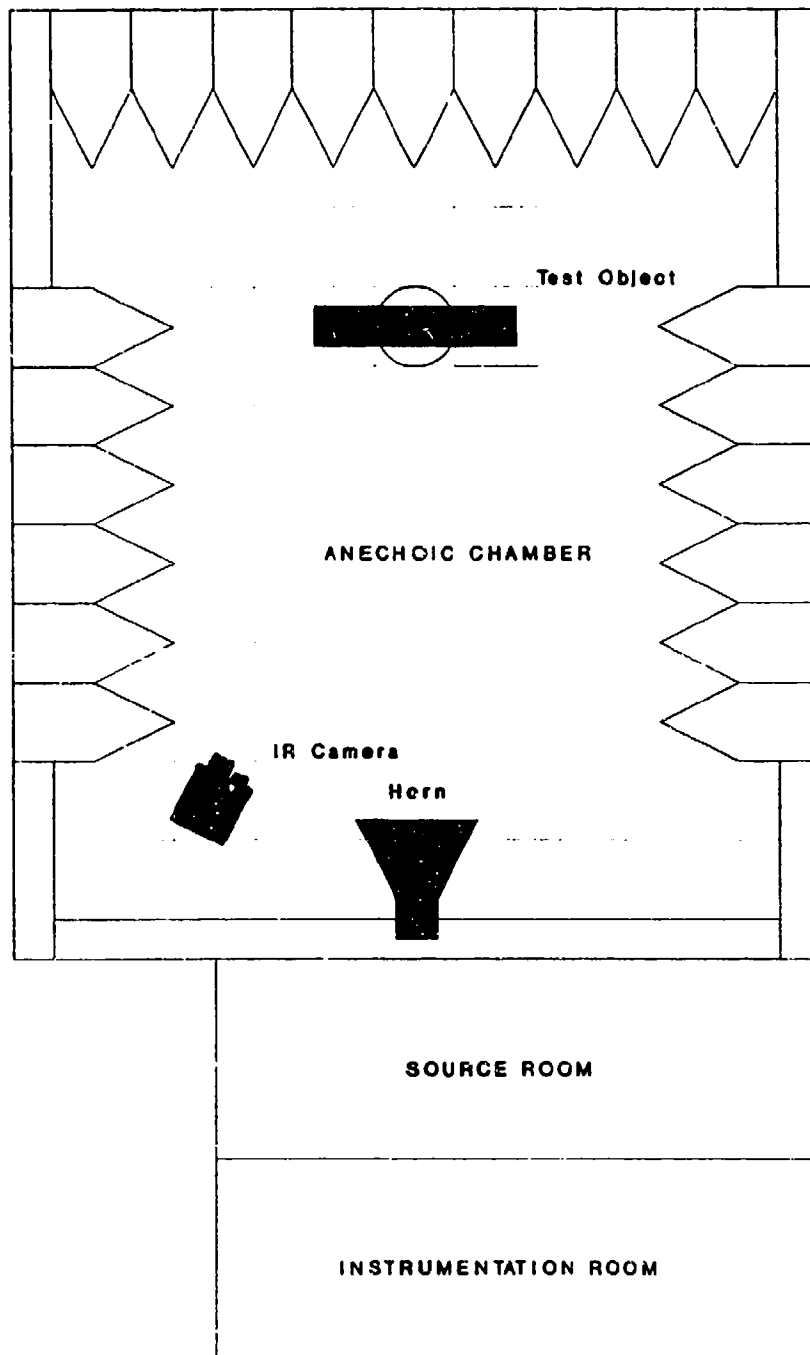
Figure 1. CU/Colorado Springs Anechoic Chamber
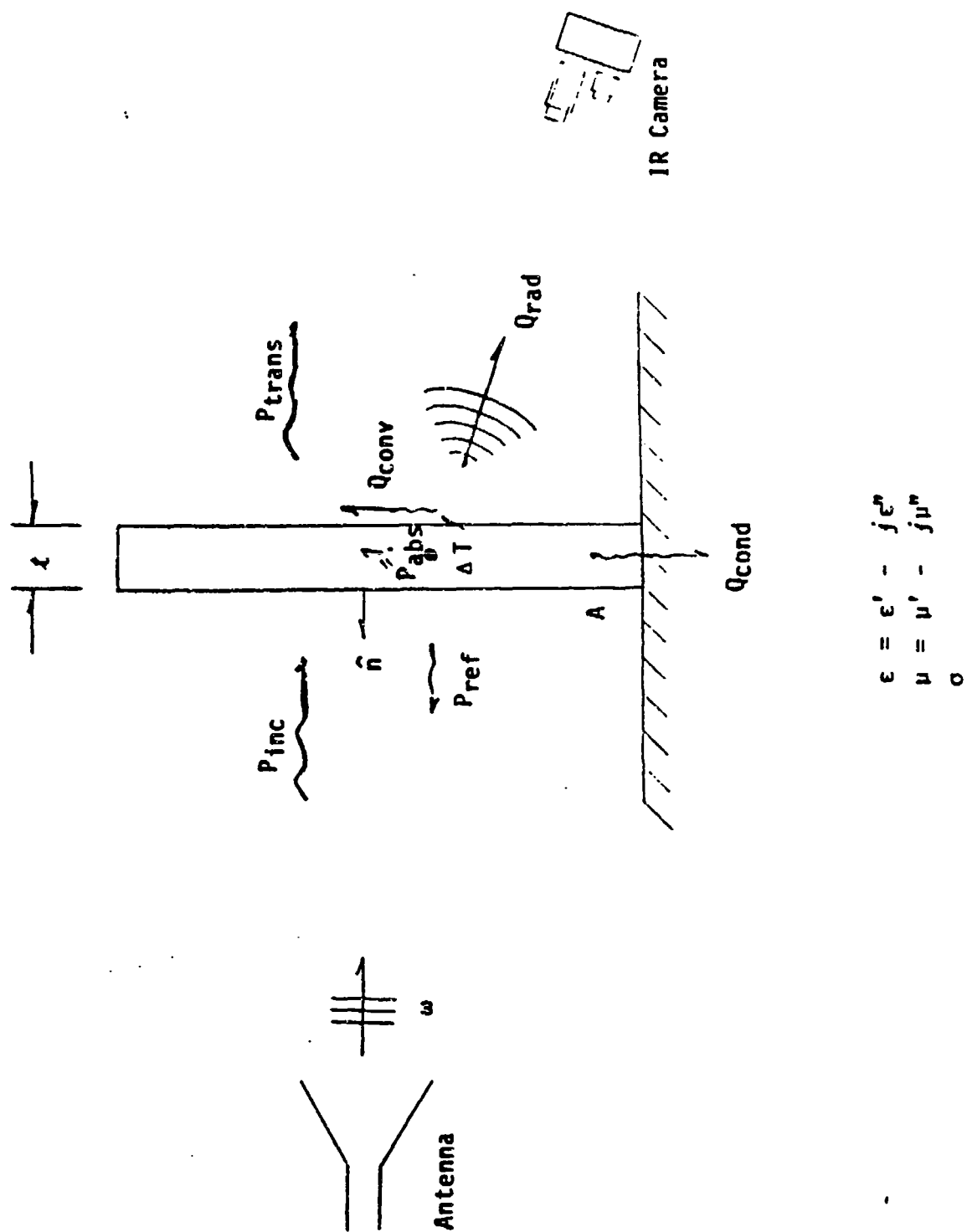
Figure 2. IR Detection Screen

Antenna

Lloyd's Mirror

(Virtual Antenna)

Detection Screen
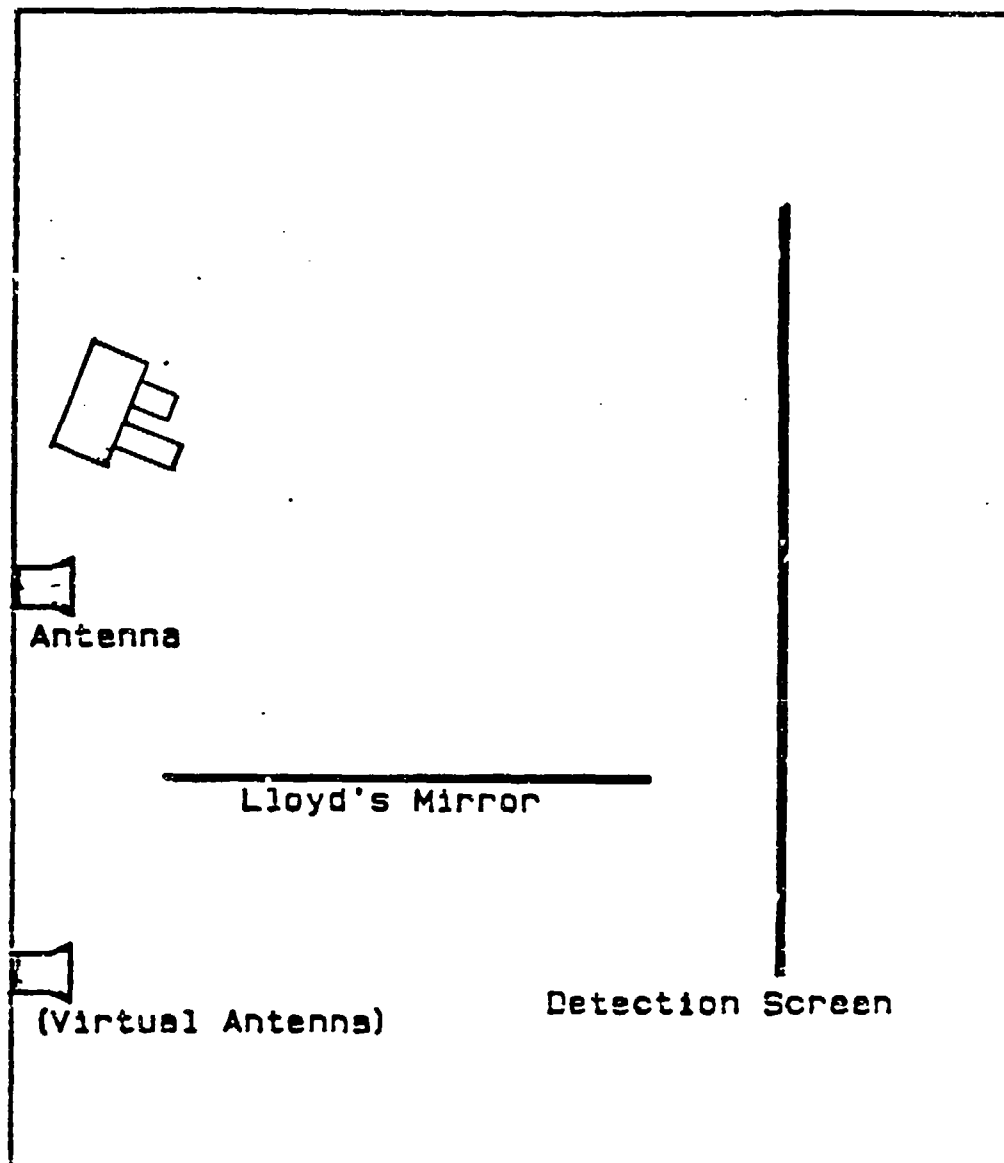
(a) Experimental Layout

Figure 3. Lloyd's Mirror Experiment
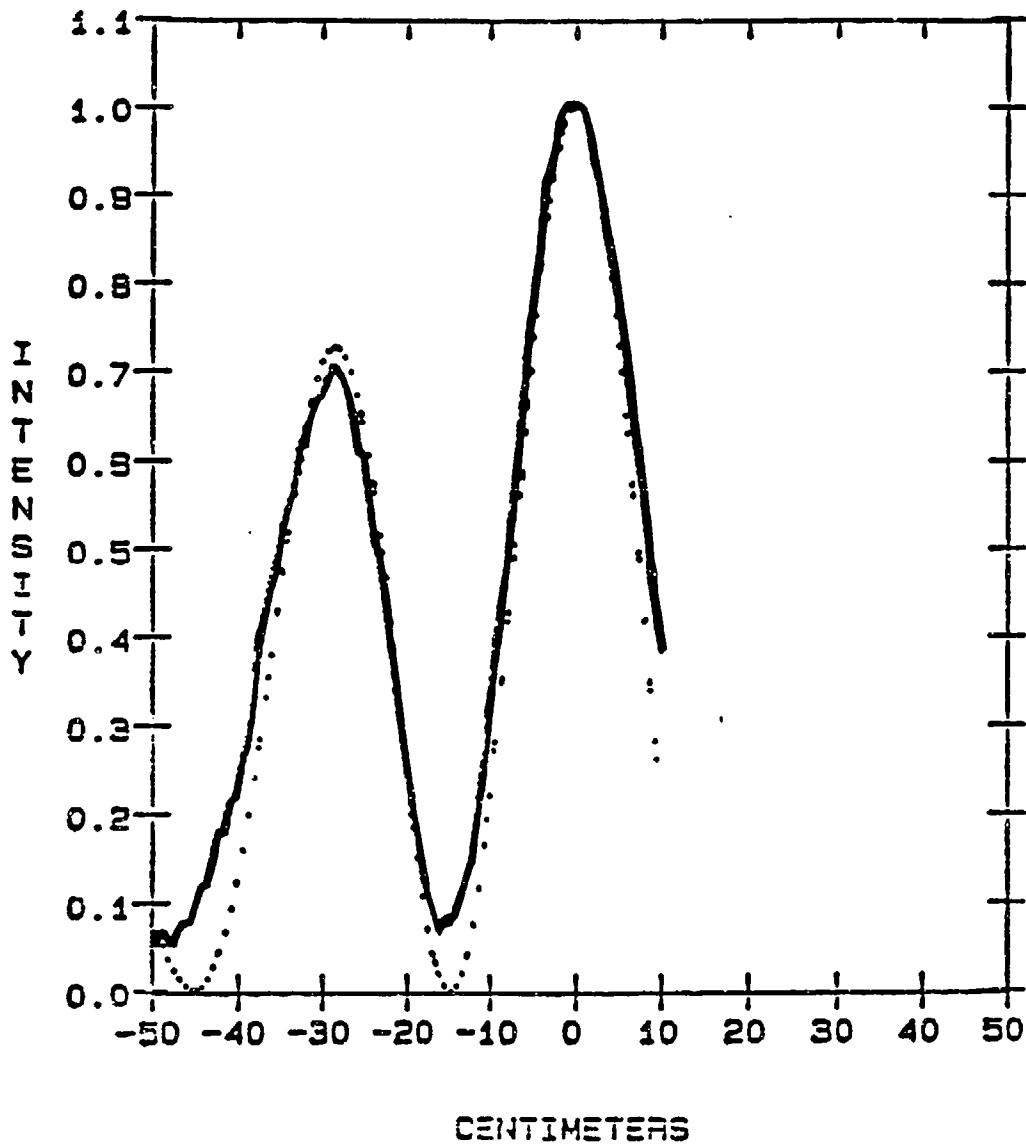
(b)   Comparison of Theoretical and Experimental Results for Lloyd's
      Mirror Experiment
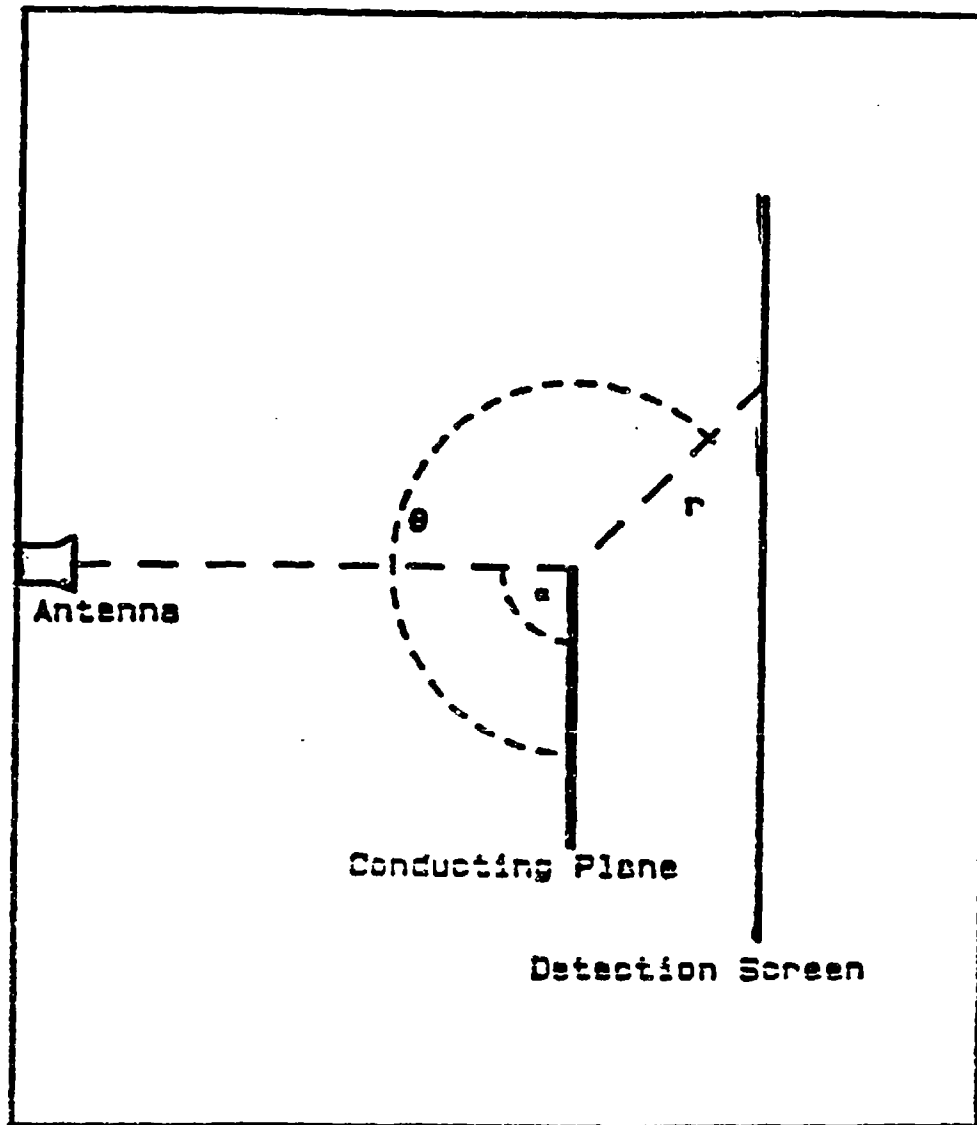
(a)   Experimental Layout

Figure 4.   Diffraction from a Half-Plane Experiment
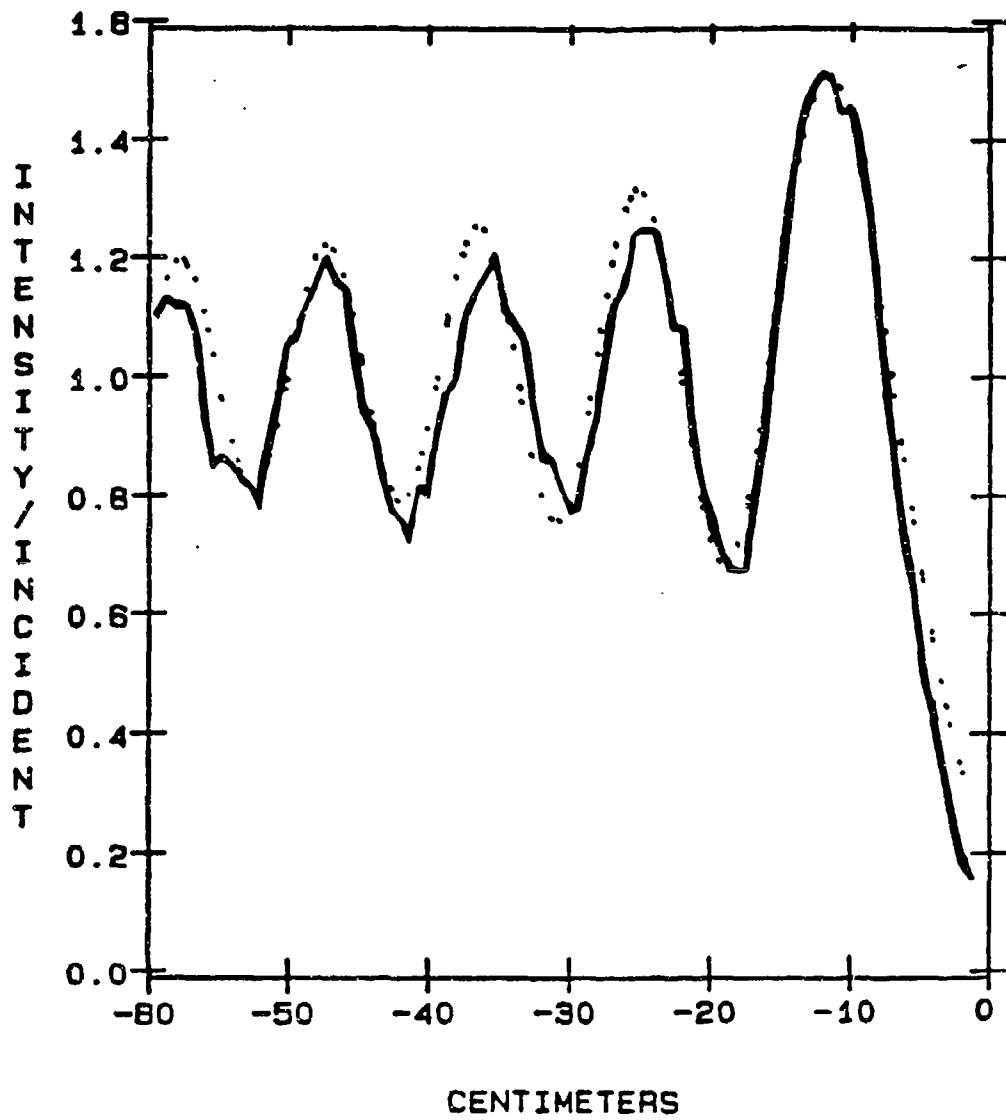
(b)   Comparison of Theoretical and Experimental Results for Half-Plane Experiment No. 1
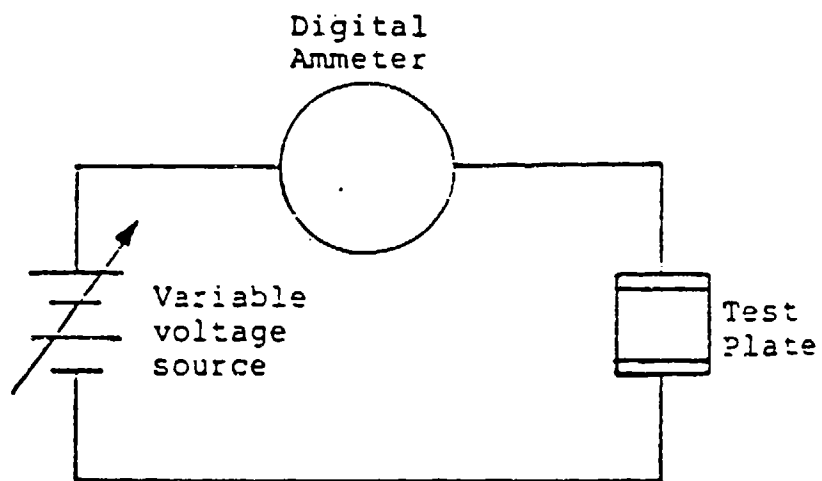
Figure 5. Simple Experimental Arrangement for Performing
Current-to-Temperature Correlations

disk: $t = 80 \ \mu m$
$\sigma = 8 \, S/m$
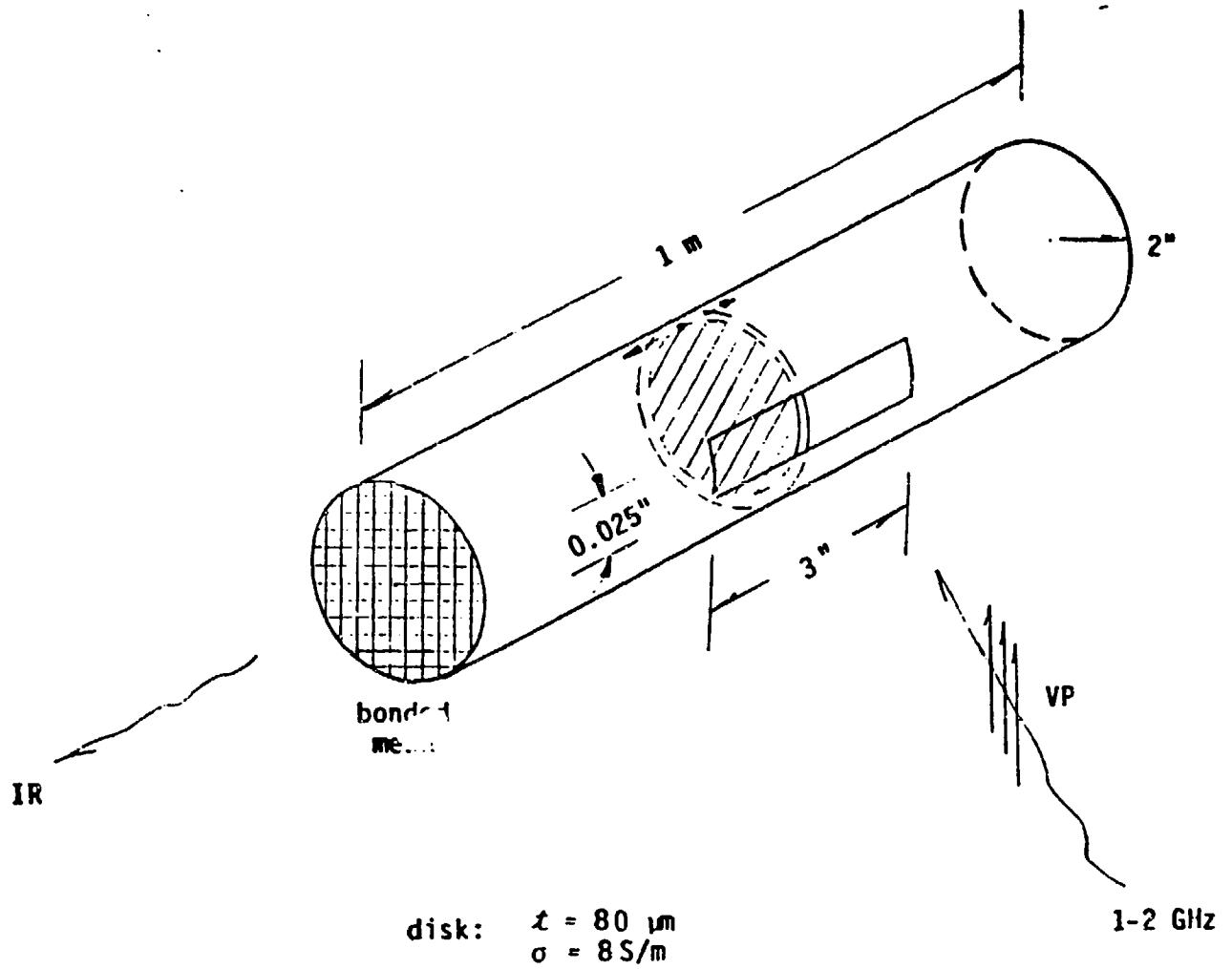
Figure 6.   Cavity/Aperture Geometry
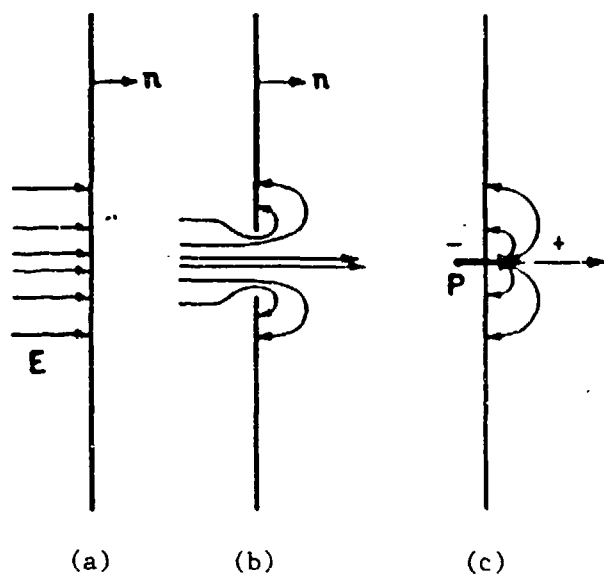
Figure 7.   Electric Field Behavior Near the Surface of a Good Conductor

(a)   Shorted Aperture: Tangential E Field Zero

(b)   Open Aperture: Normal E Field Penetration

(c)   Open Aperture: Equivalent Normal Electric Dipole Moment
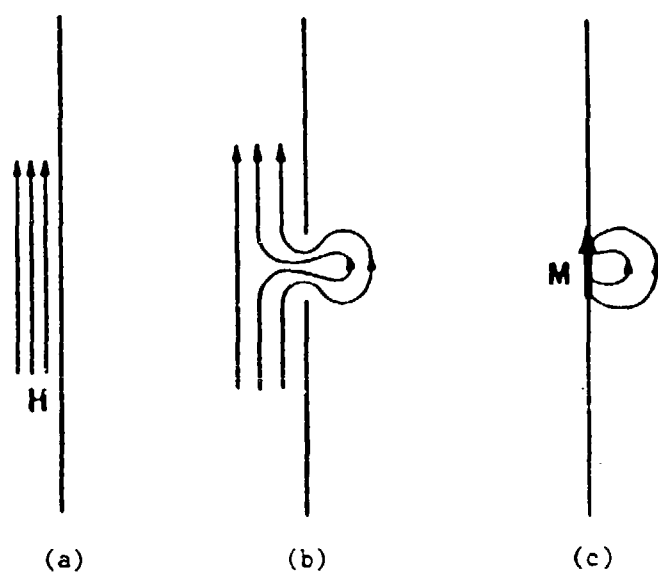
Figure 8.   Magnetic Field Behavior Near the Surface of a Good Conductor

(a)   Shorted Aperture: Normal B Field Zero

(b)   Open Aperture: Tangential B Field Penetration

(c)   Open Aperture: Equivalent Tangential Magnetic Dipole Moment

46
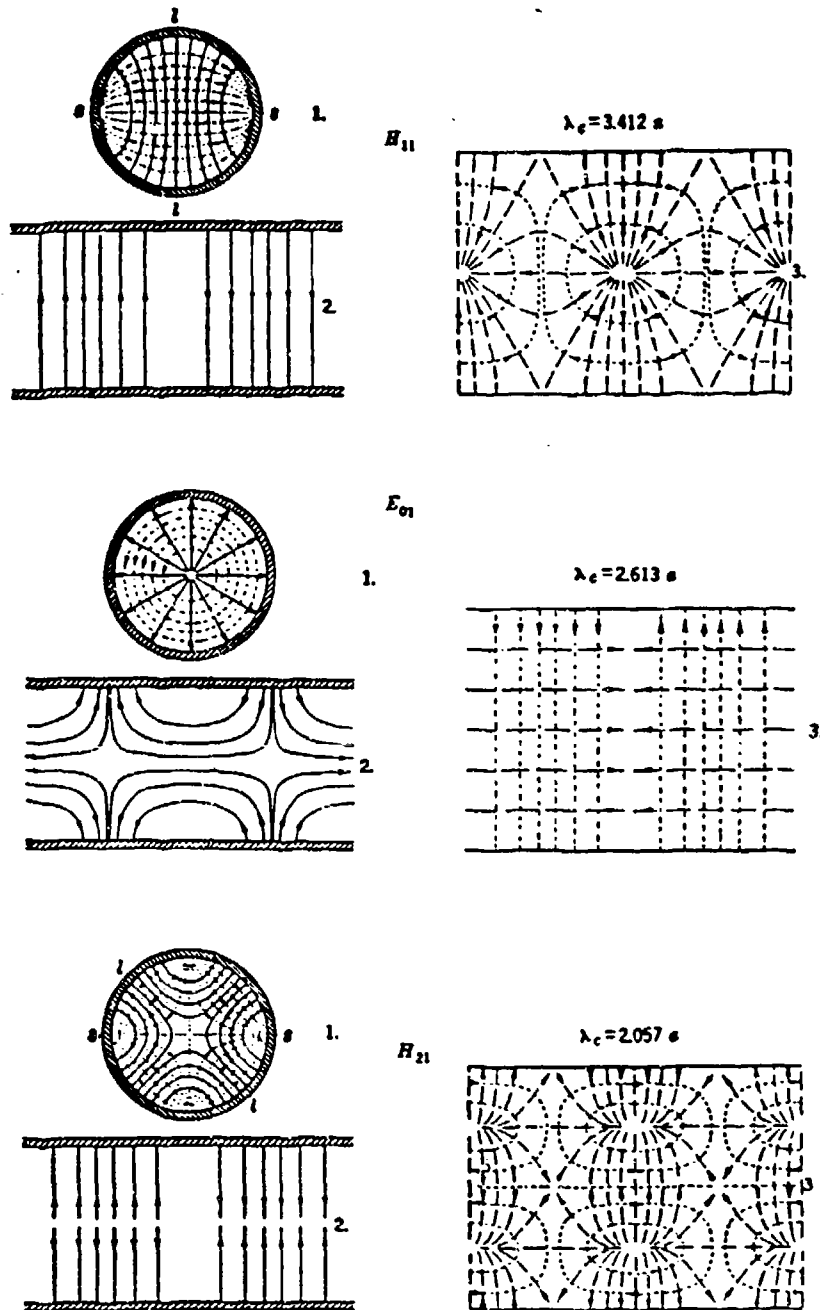
Figure 9.   Lowest Order Circular Cylindrical Waveguide Modes
(From: Marcuvitz, Waveguide Handbook)

Figure 10. Cross-Sectional Relief Maps and Isothermal Equi-Contour Plots
of the Thermograms of the Interior Cylindrical Field at 1.75 GHz

(a)   Detection Screen at Center of Aperture Slit

(b)   Detection Screen at 1.0 cm from Center of Aperture Slit

(c)   Detection Screen at 1.5 cm from Center of Aperture Slit

(d)   Detection Screen at 2.0 cm from Center of Aperture Slit

(e)   Detection Screen at 2.5 cm from Center of Aperture Slit

(f)   Detection Screen at 3.0 cm from Center of Aperture Slit

(g)   Detection Screen at 3.5 cm from Center of Aperture Slit

(h)   Detection Screen at 4.0 cm from Center of Aperture Slit

(i)   Detection Screen at 4.5 cm from Center of Aperture Slit

(j)   Detection Screen at 5.0 cm from Center of Aperture Slit

(k)   Detection Screen at 5.5 cm from Center of Aperture Slit

(l)   Detection Screen at 23.0 cm from Center of Aperture Slit

(m)   Detection Screen at 30.0 cm from Center of Aperture Slit

(n)   Detection Screen at 1/4 lambda from Center of Aperture Slit
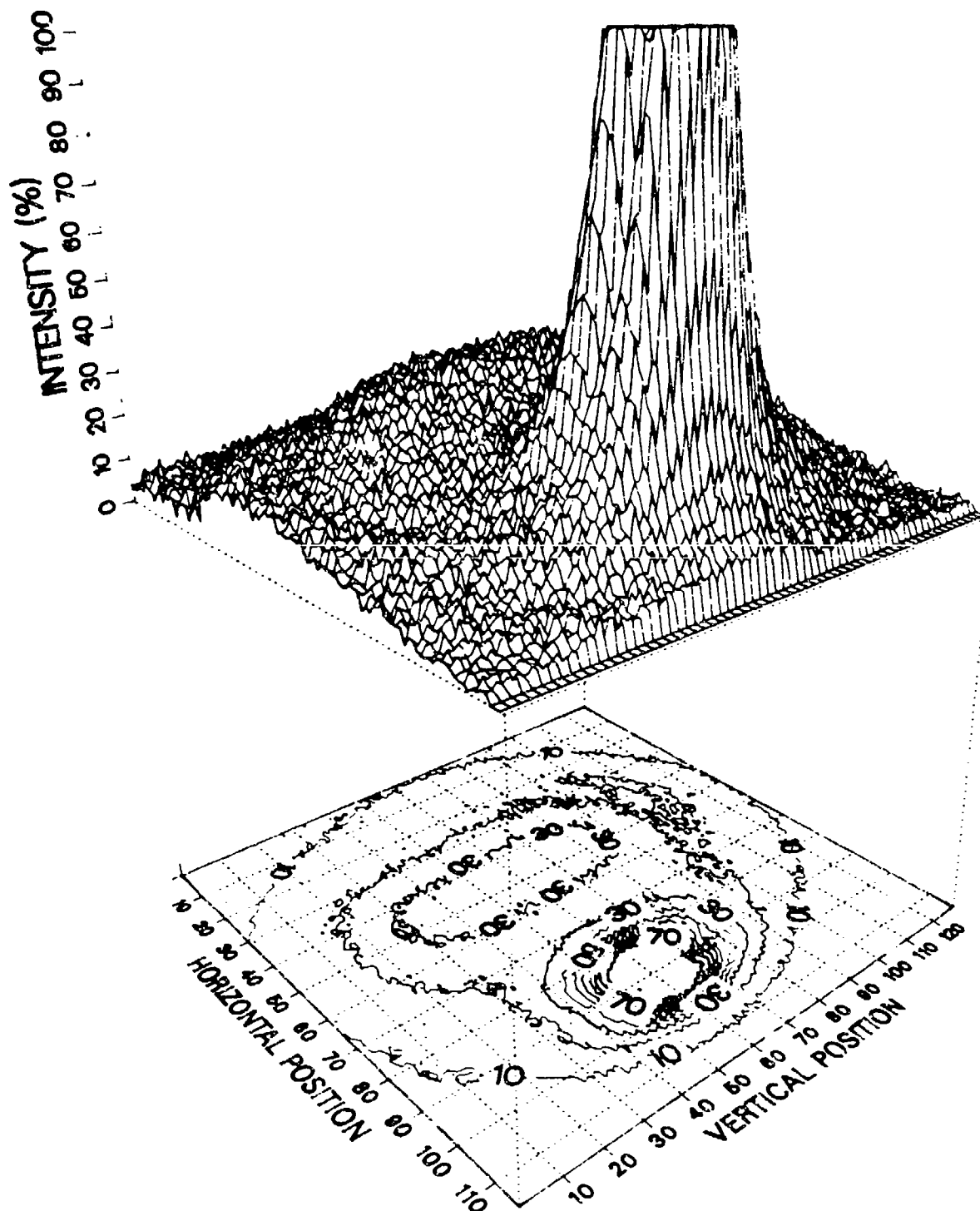
# Screen at slit center, 1.75GHz
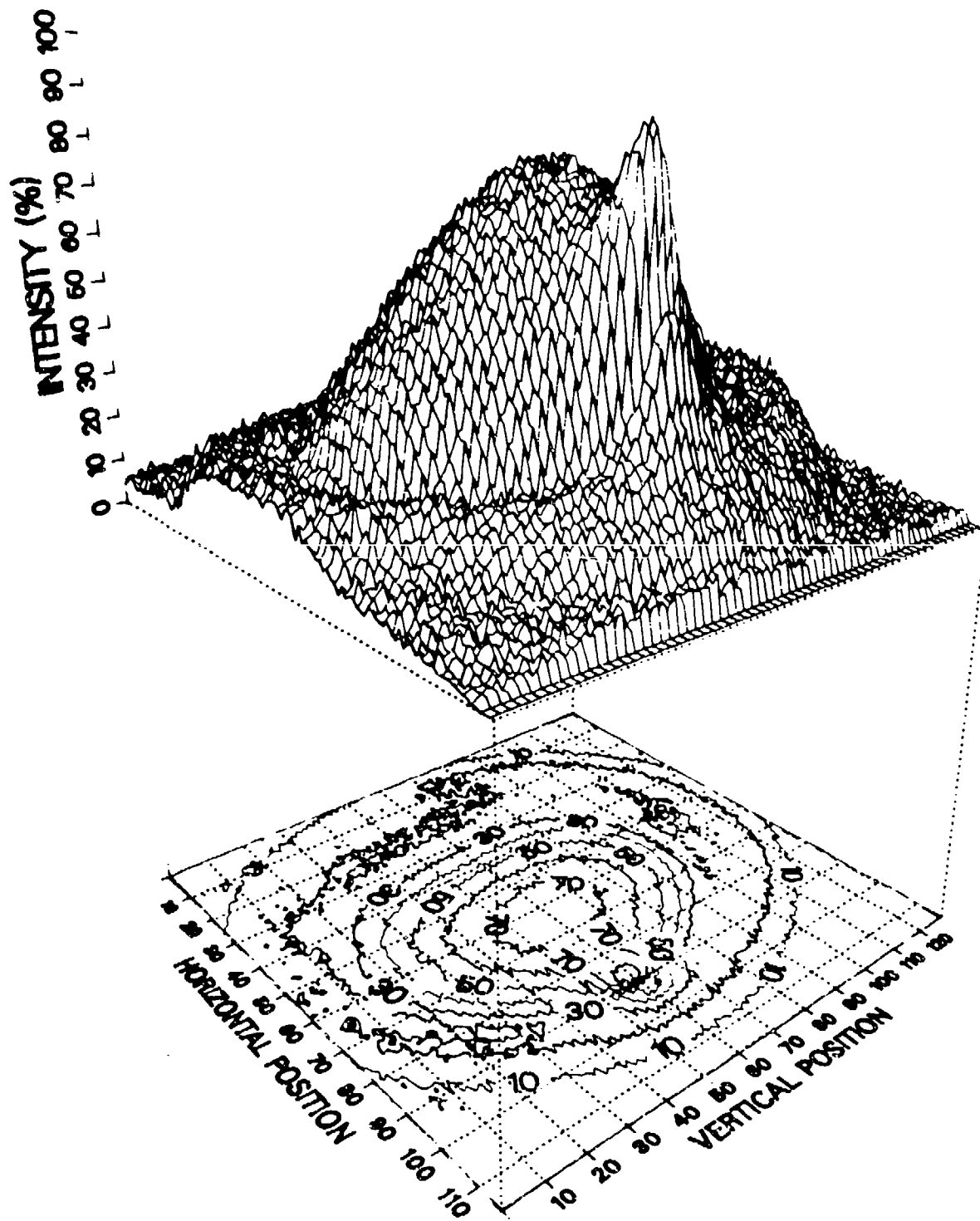
(a)

Screen 1cm from slit center, 1.75GHz
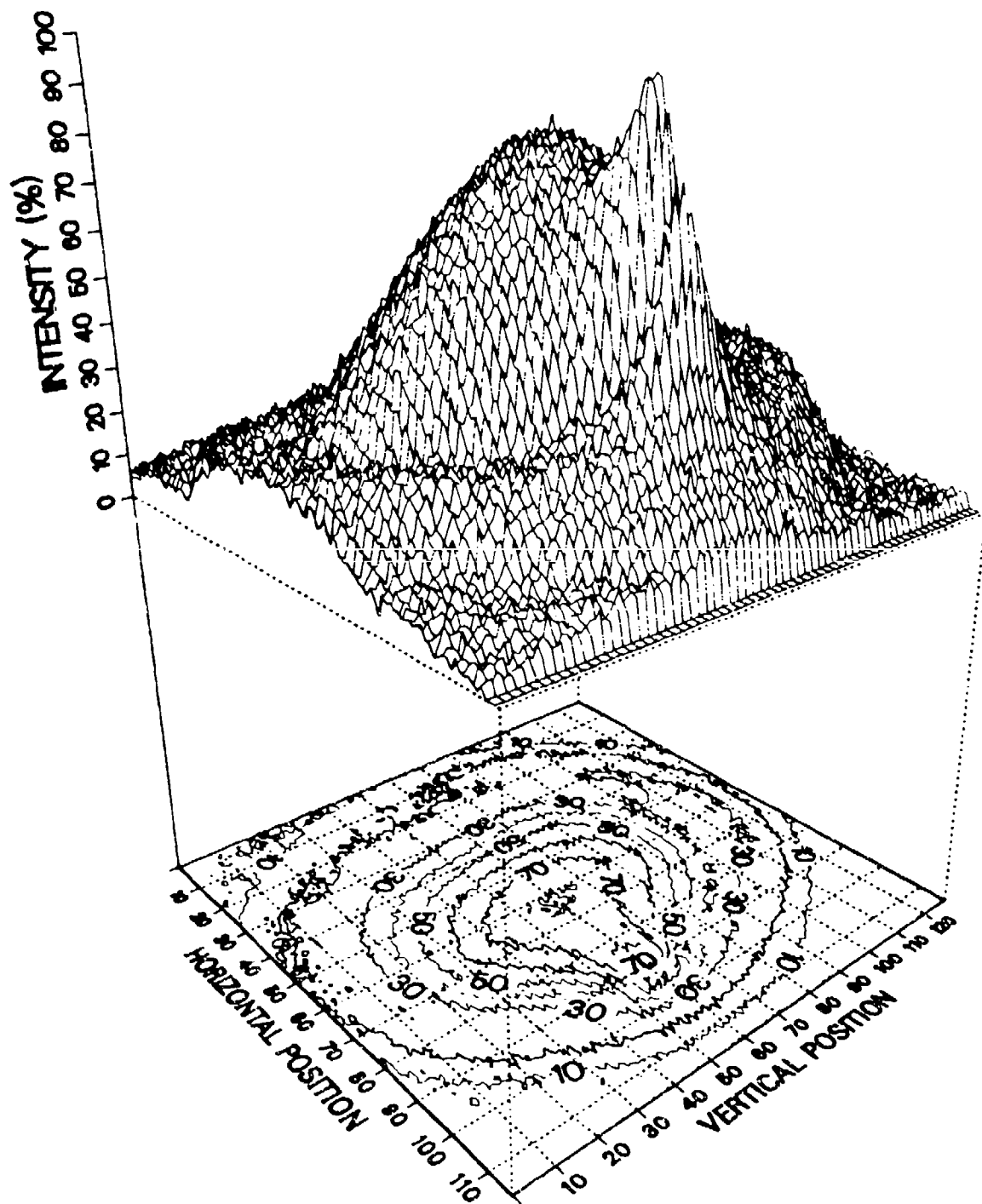
(b)

Screen 1.5cm from slit center, 1.75GHz
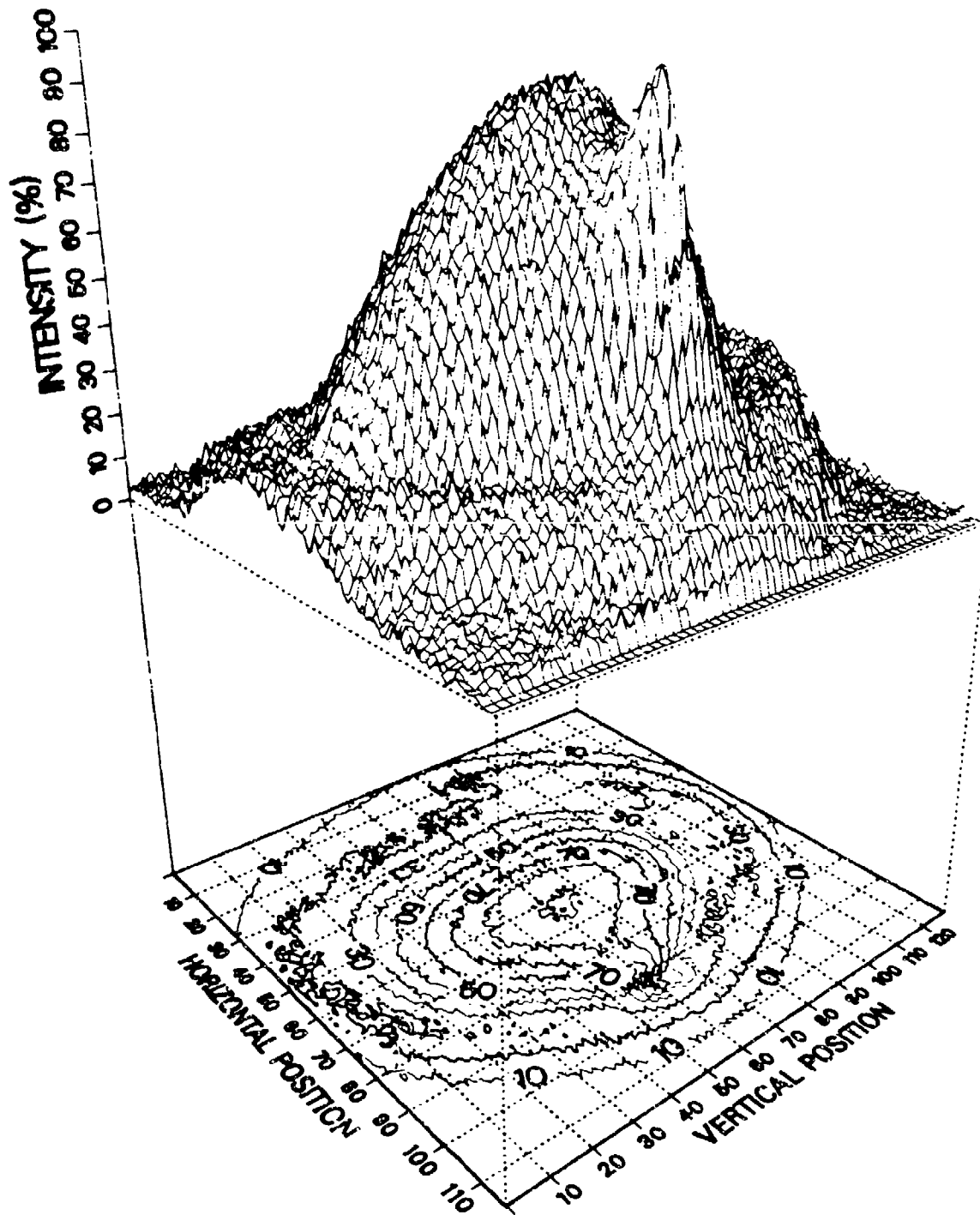
(c)

Screen 2cm from slit center, 1.75GHz

(d)

Screen 2.5cm from slit center, 1.75GHz

(e)
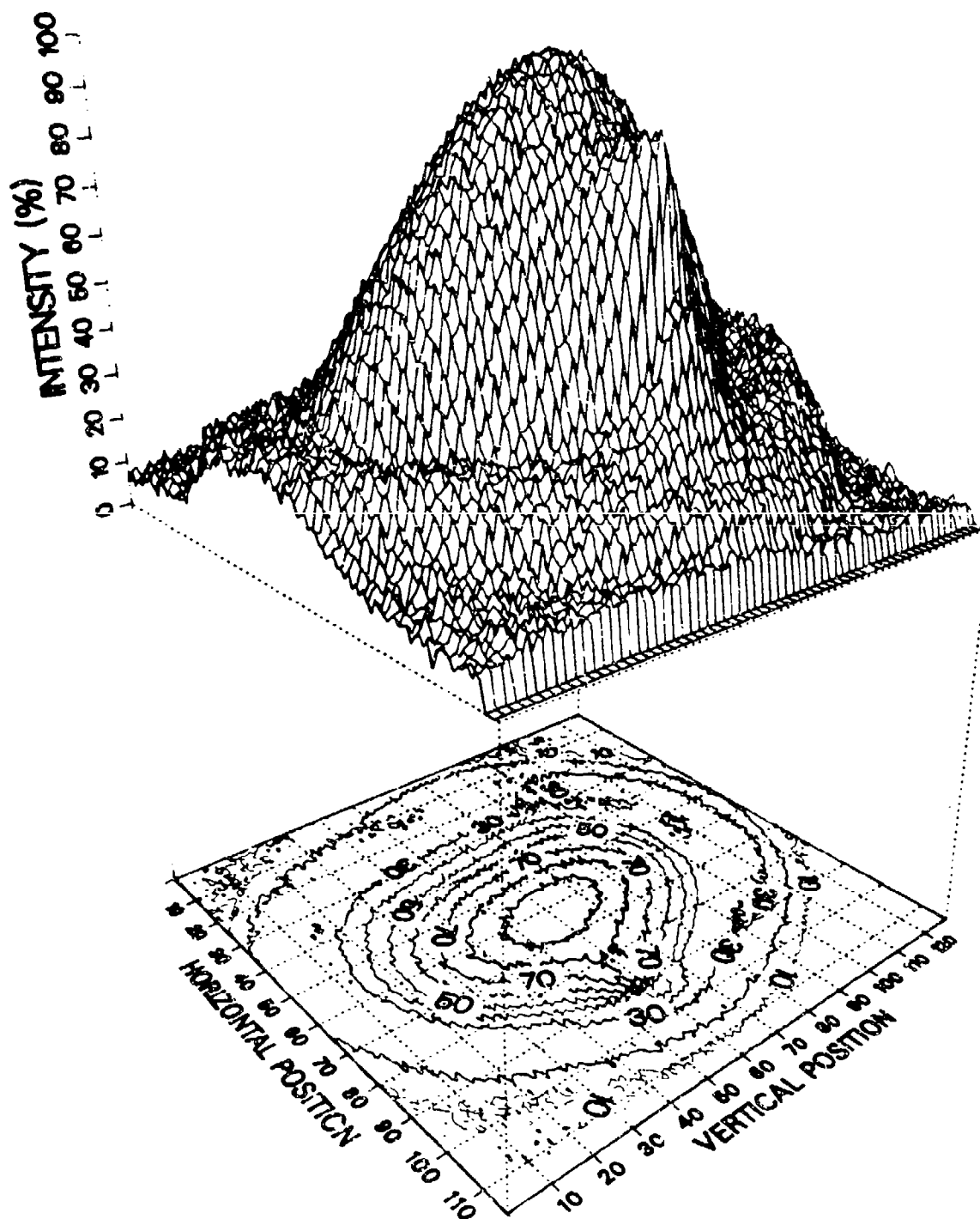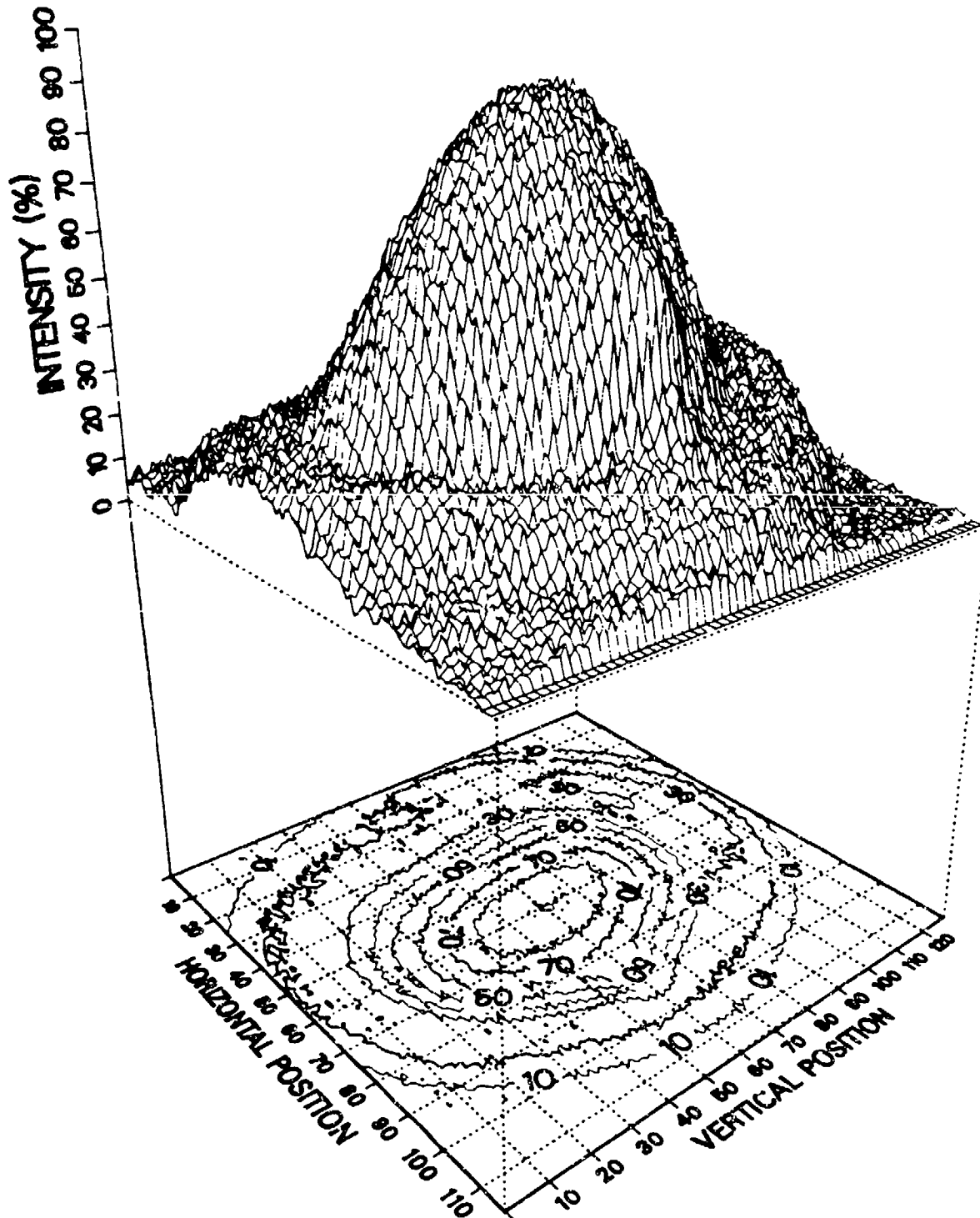
Screen 3cm from slit center, 1.75GHz
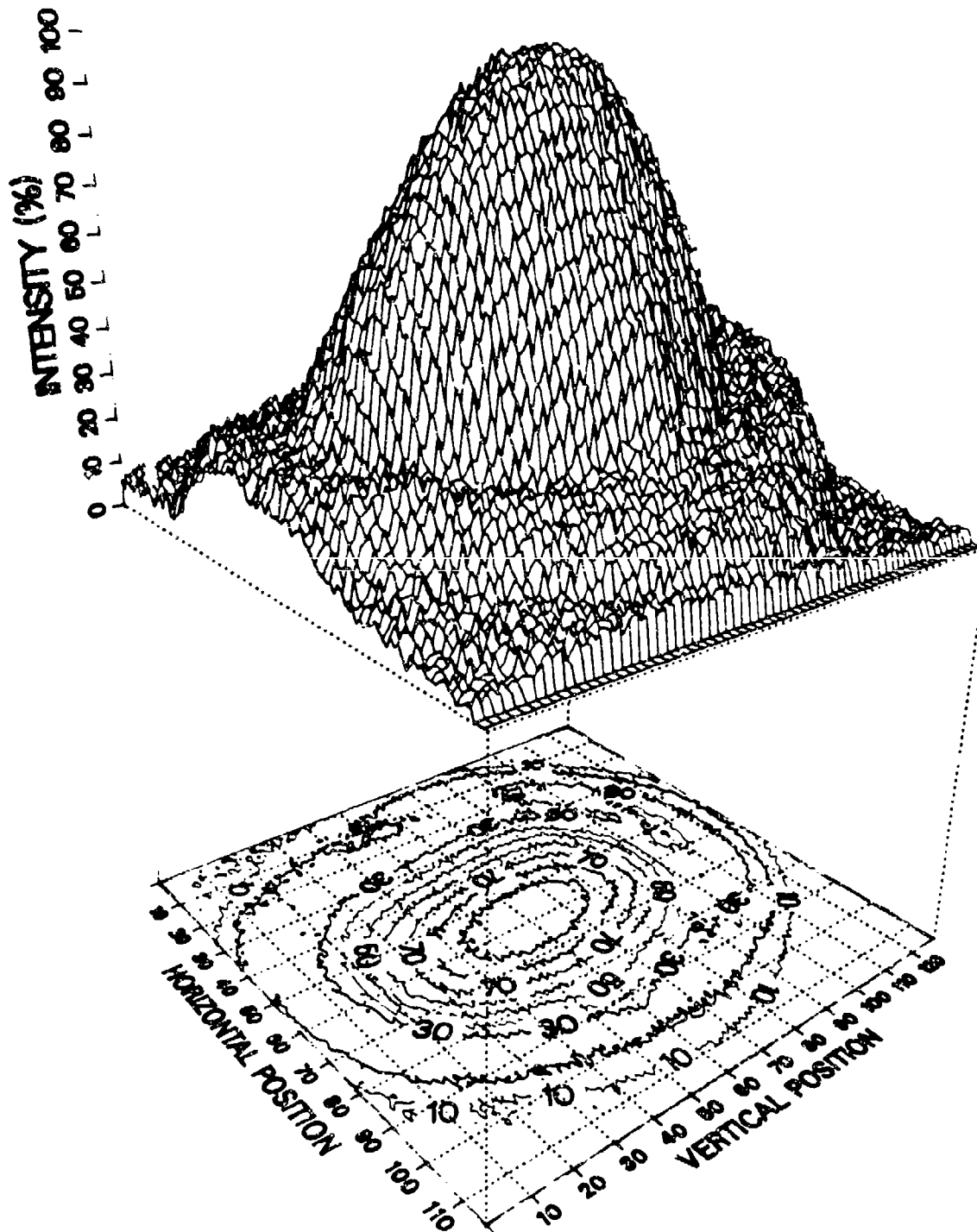
(f)

Screen 3.5cm from slit center, 1.75GHz

(g)

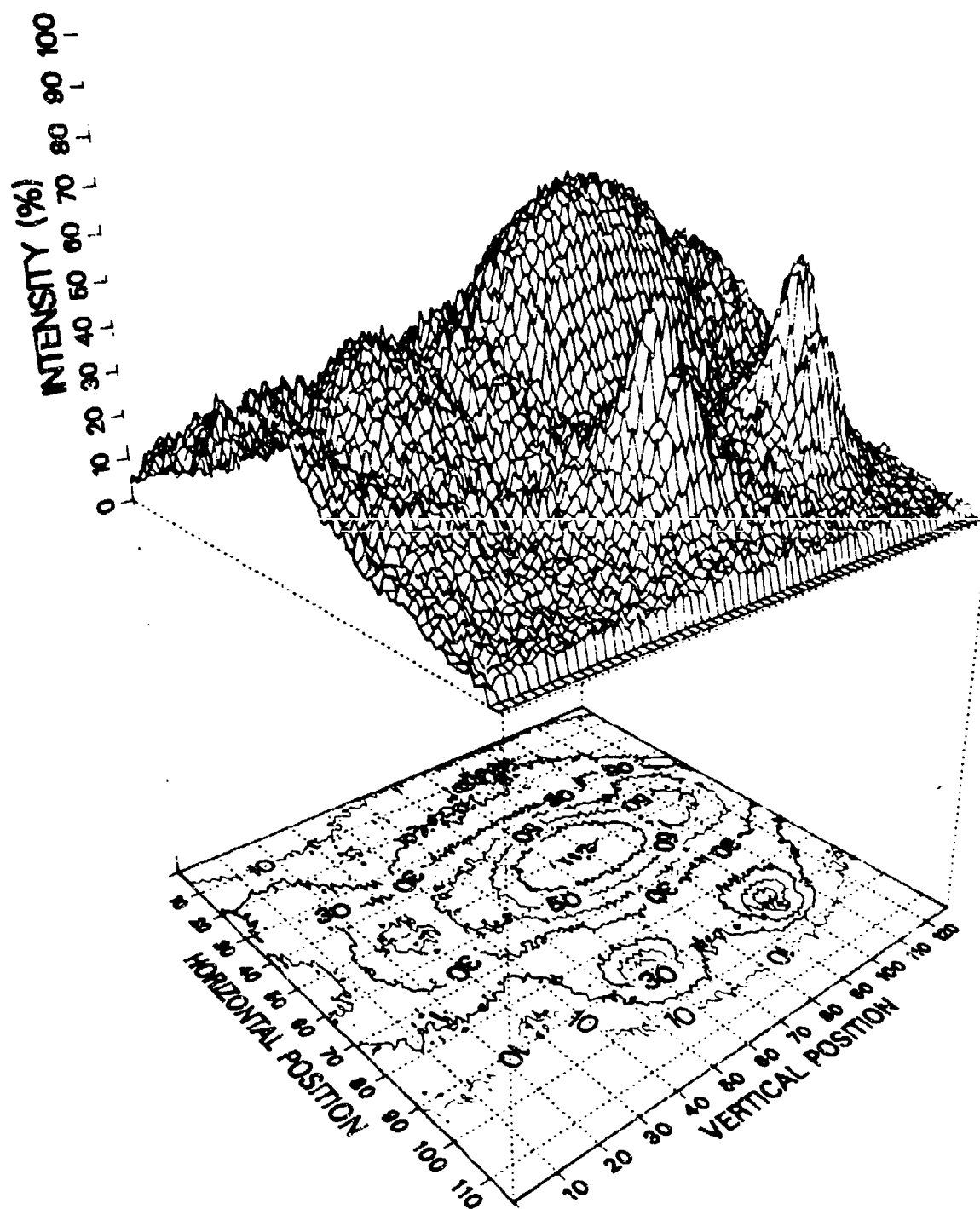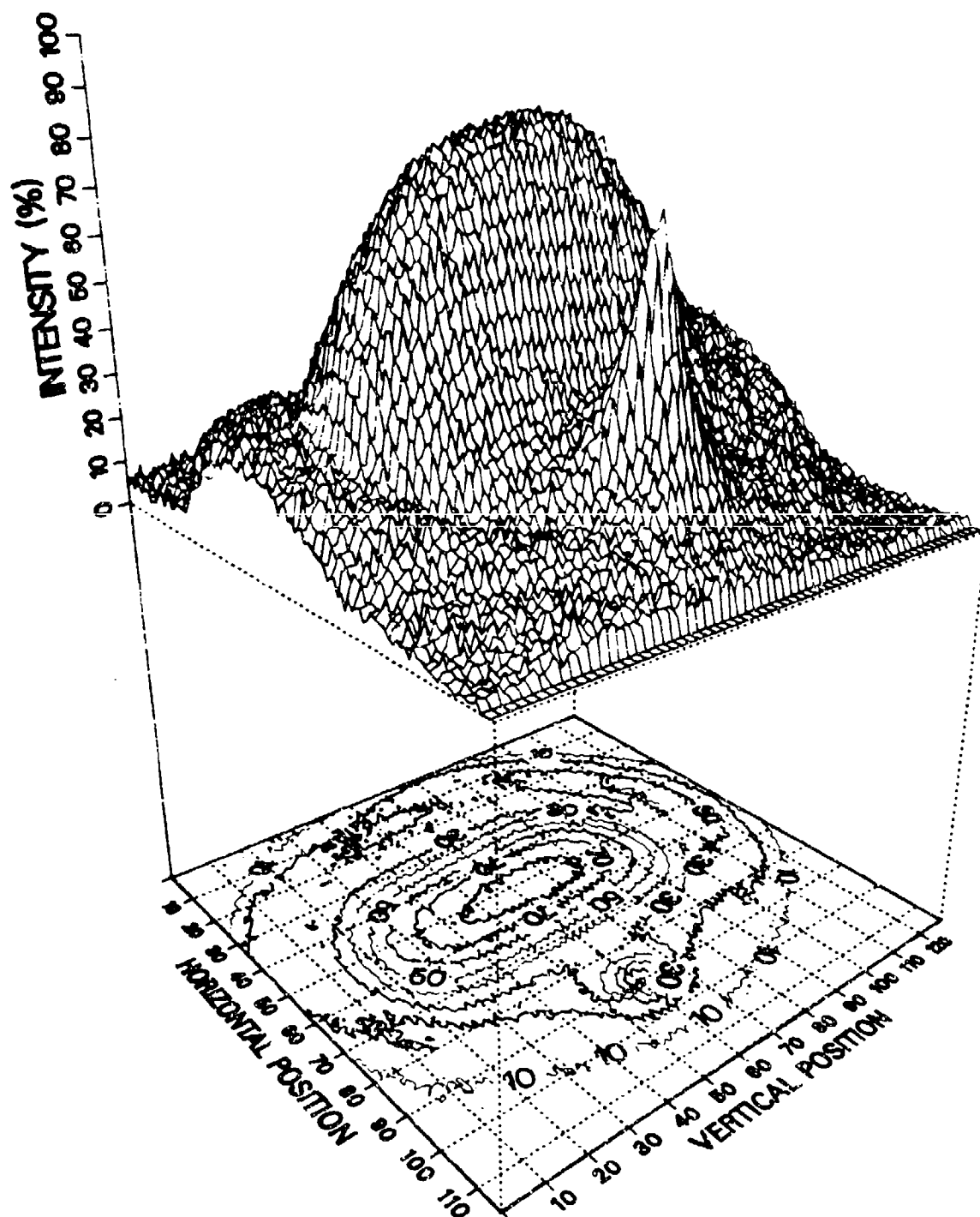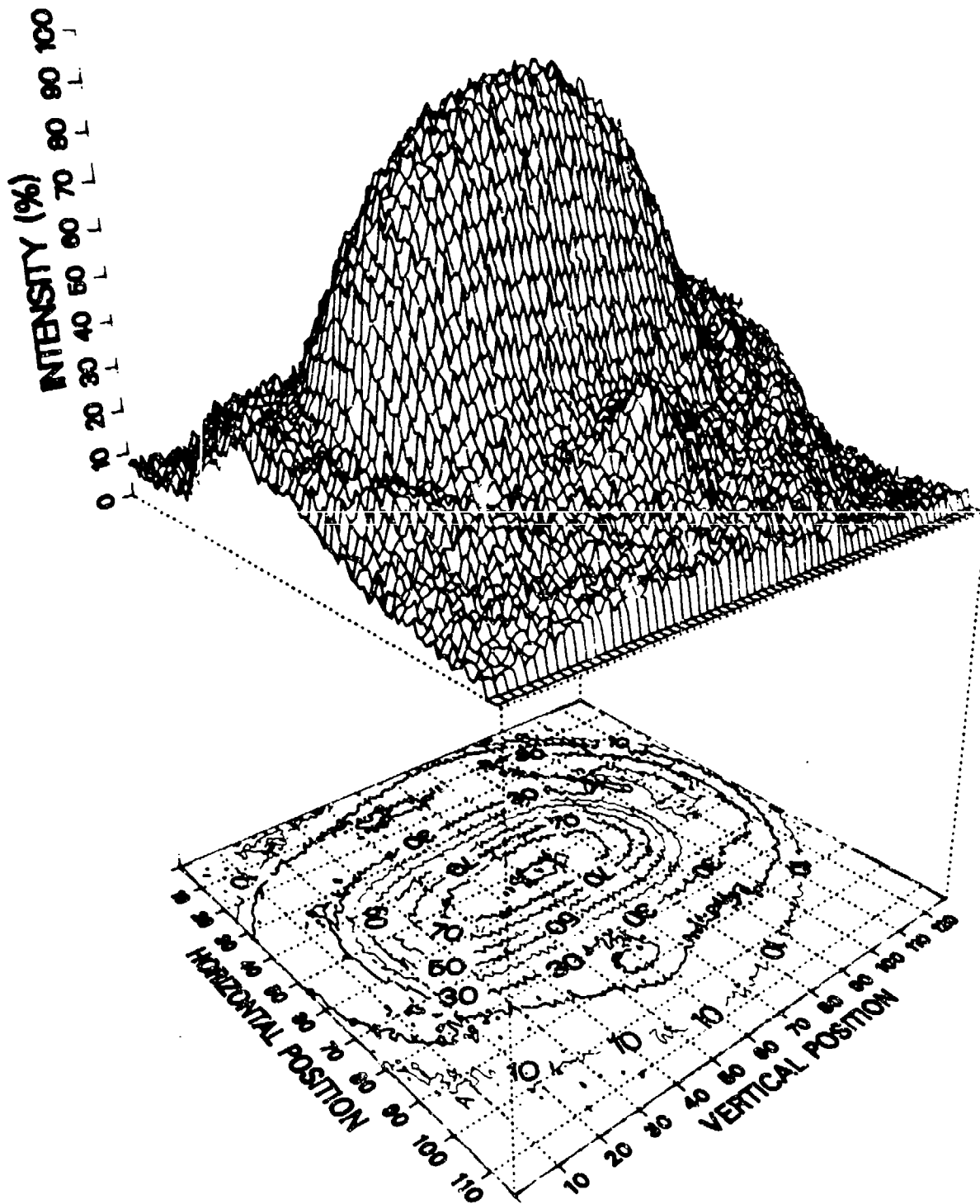# Screen 4cm from slit center, 1.75GHz

(h)
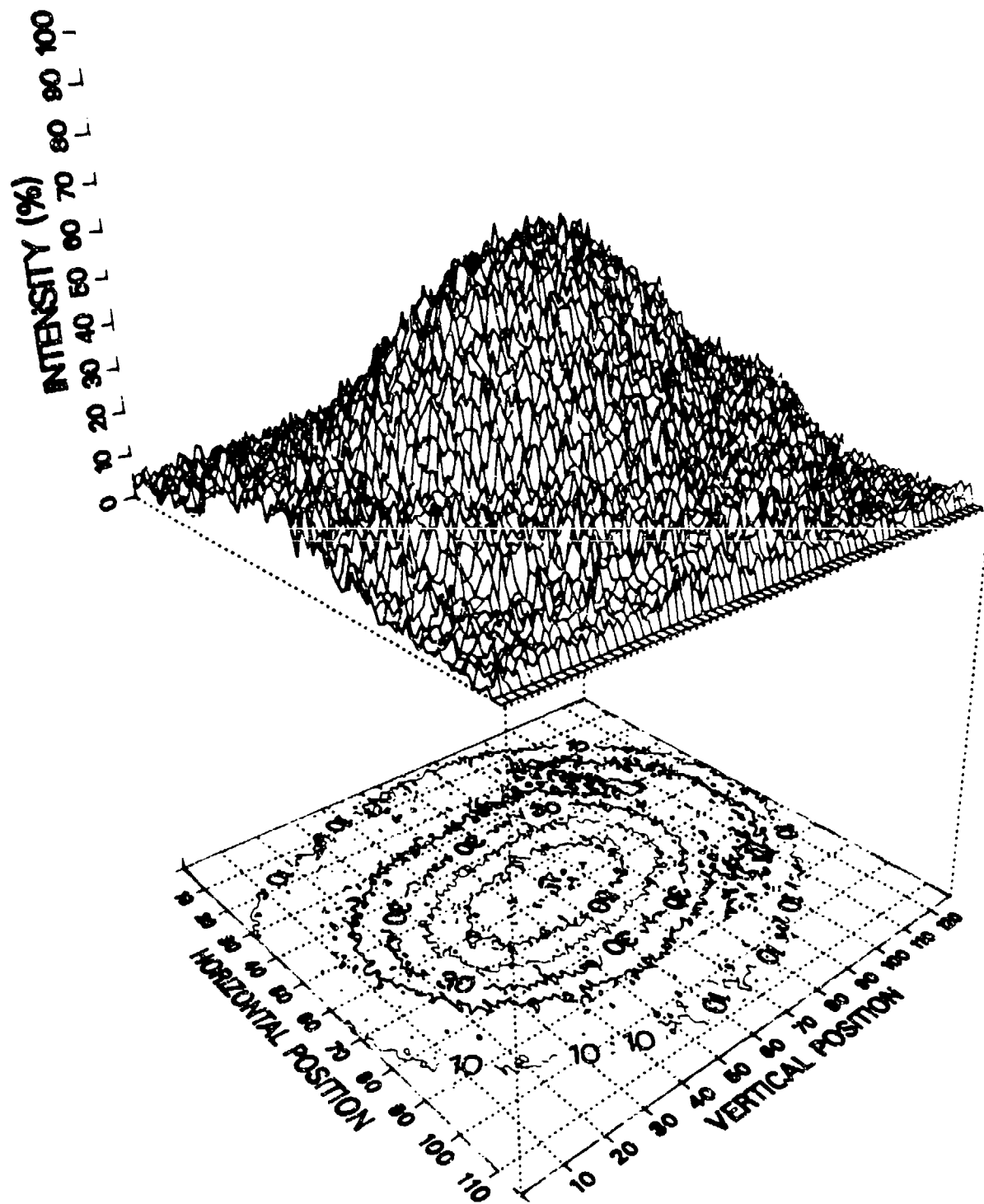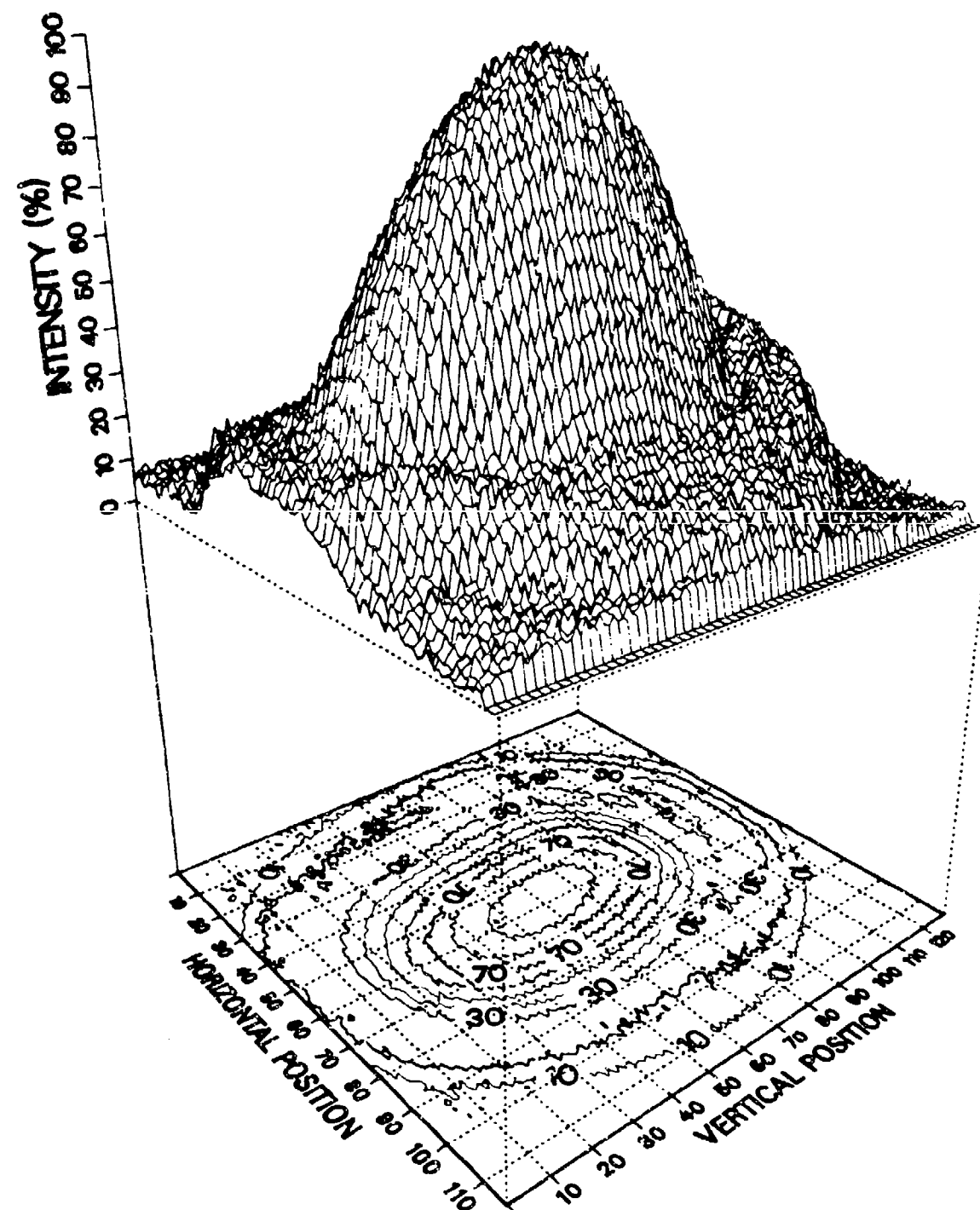
Screen 4.5cm from slit center, 1.75GHz
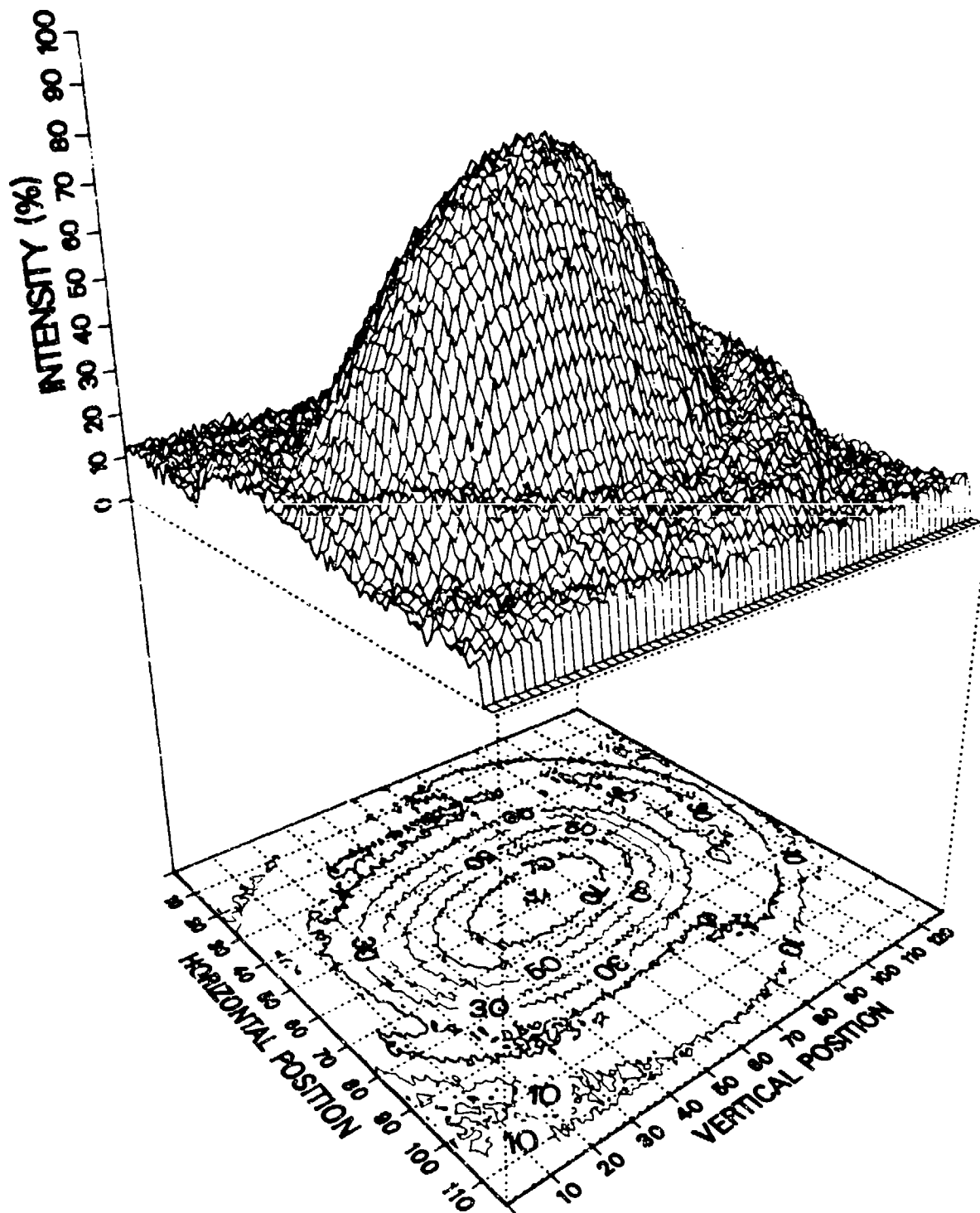
Screen 5cm from slit center, 1.75GHz
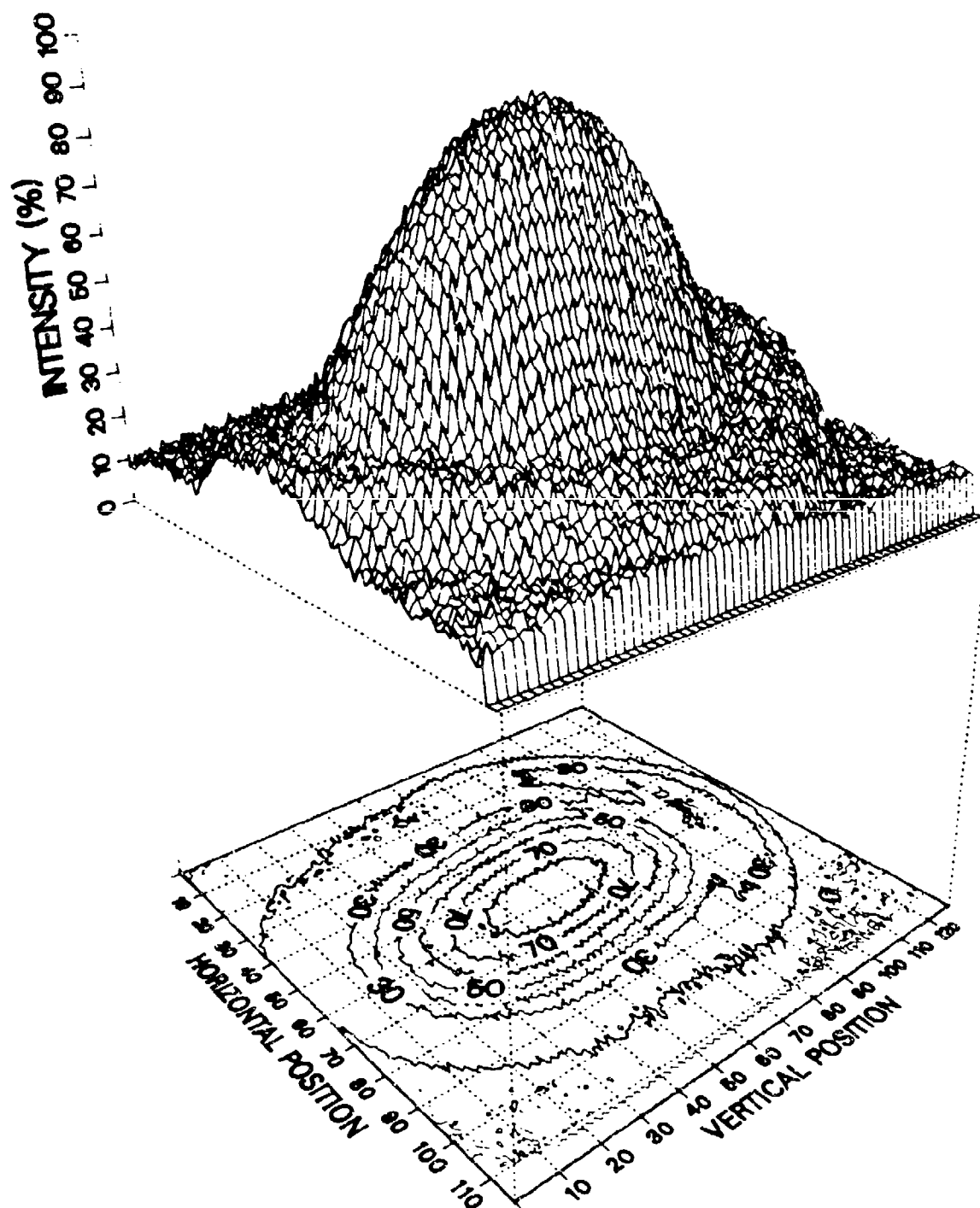
Screen 5.5cm from slit center, 1.75GHz
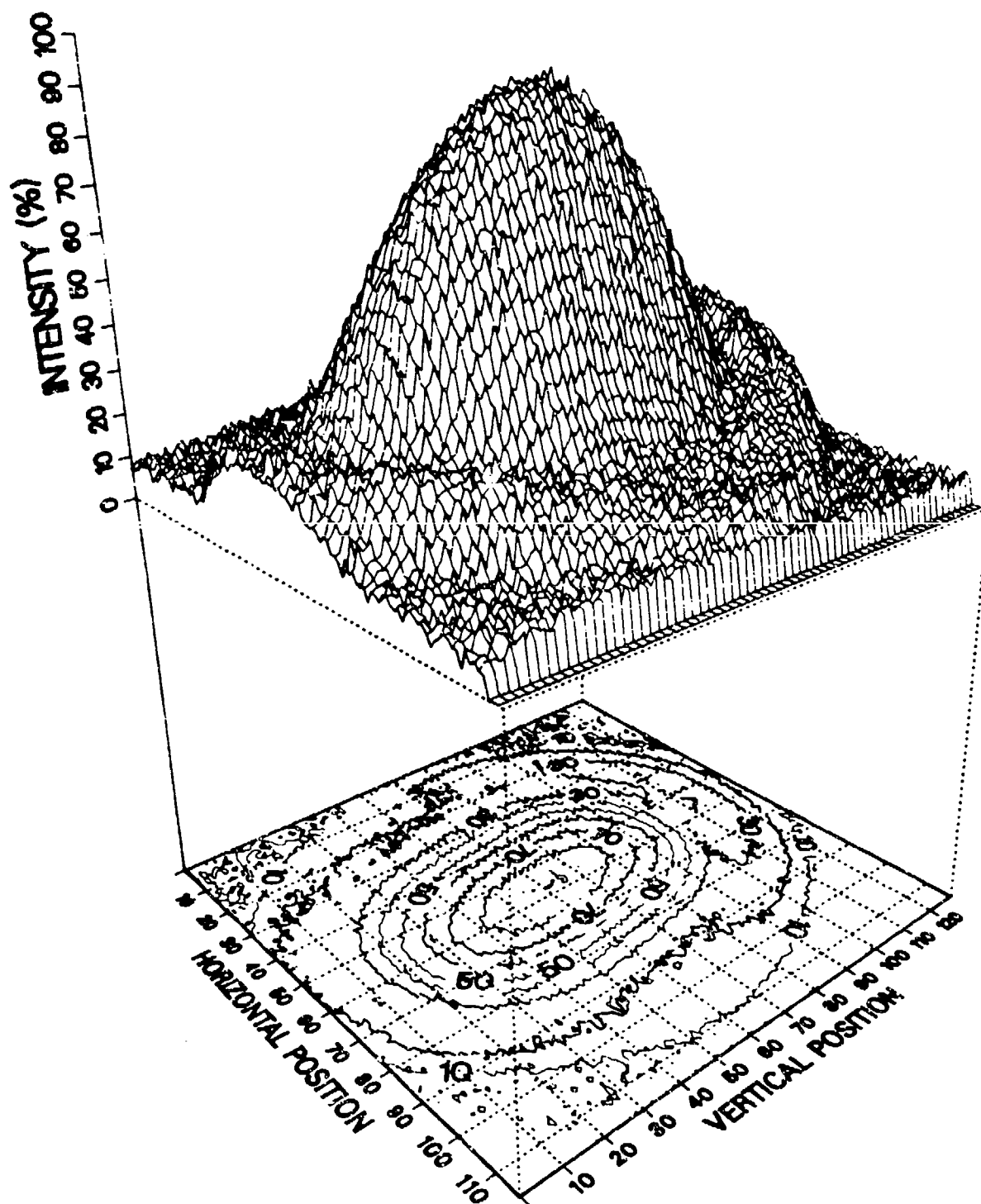
(k)

Screen 23cm from slit center, 1.75GHz
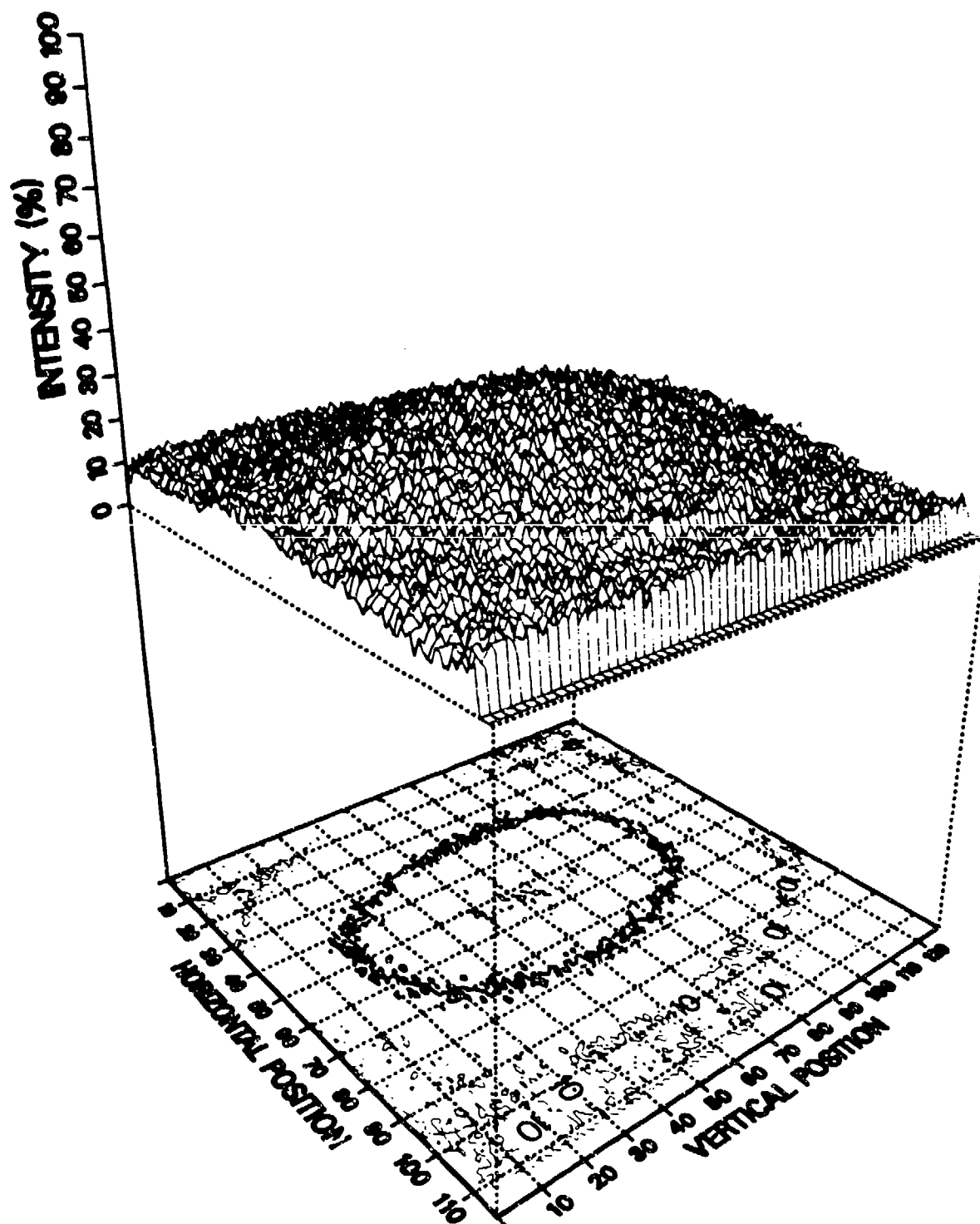
Screen 30cm from slit center, 1.75GHz

Screen 1/4 lambda from slit center, 1.75GHz

(n)
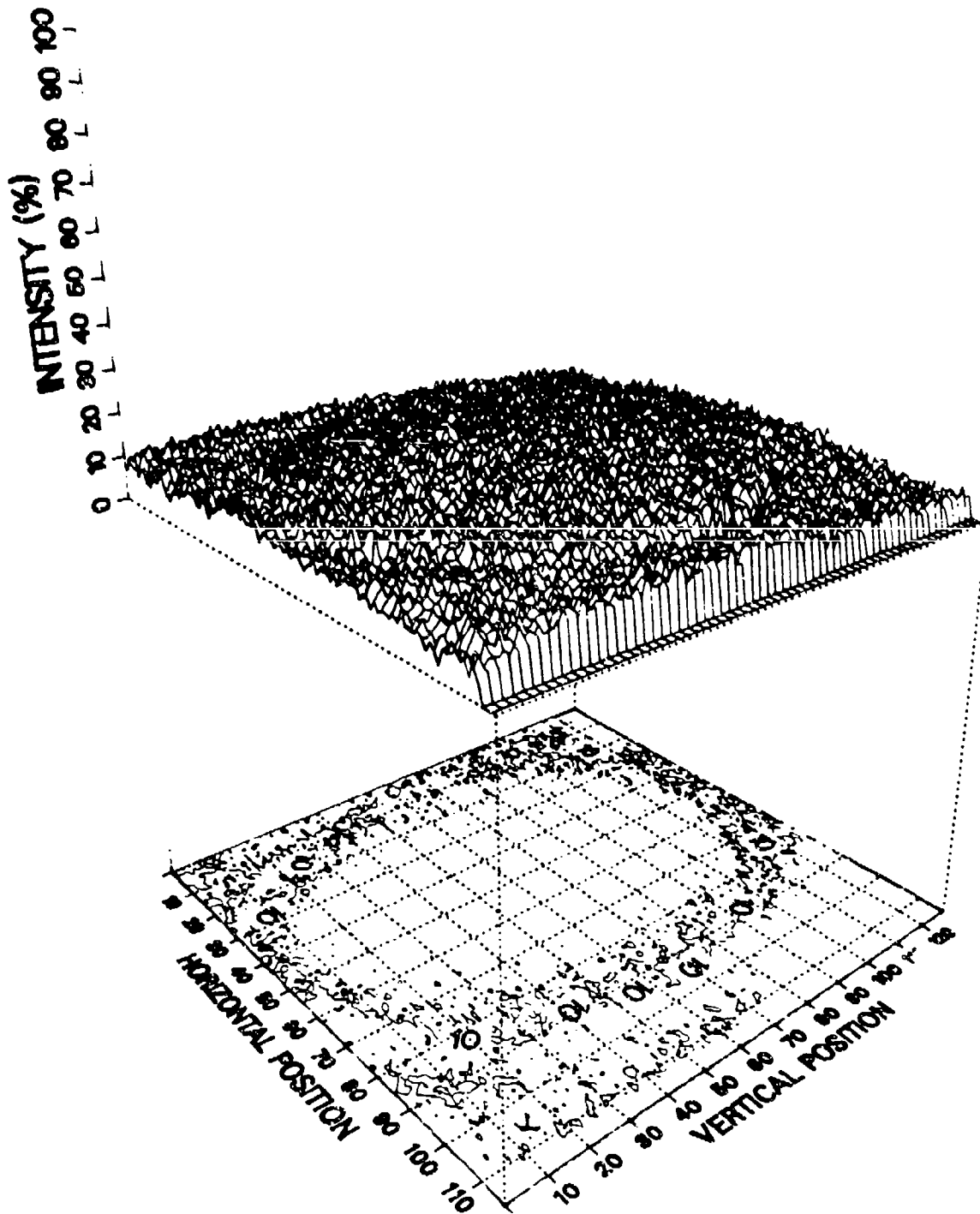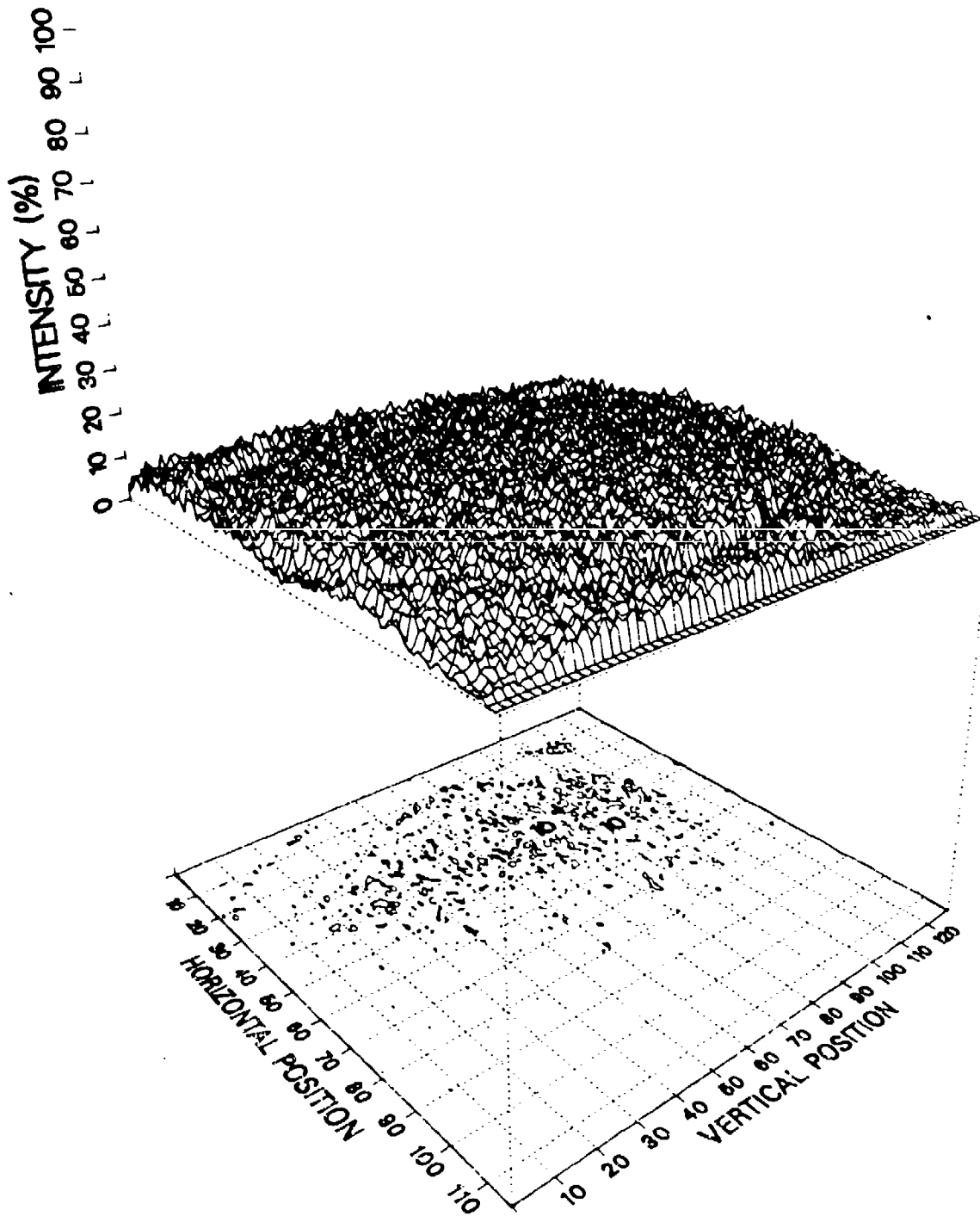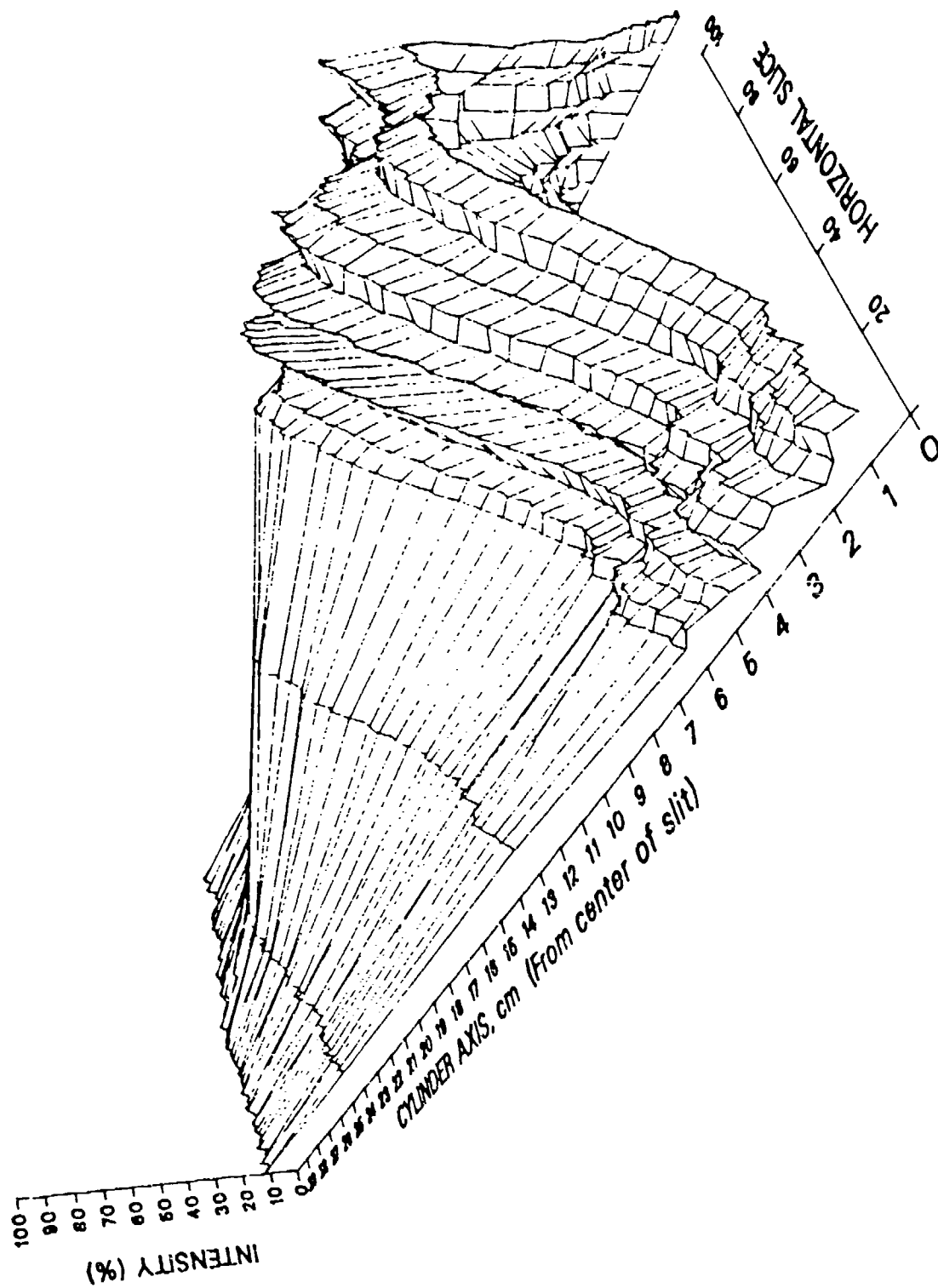
Figure 11. Longitudinal Relief Map of the Thermogram of the Interior Cylindrical Field at 1.75 GHz Taken Through the Middle of the Cylinder

Figure 12. Cross-Sectional Relief Maps and Isothermal Equi-Contour Plots
of the Thermograms of the Interior Cylindrical Field at 1.965 GHz

(a)   Detection Screen at Center of Aperture Slit

(b)   Detection Screen at 0.5 cm from Center of Aperture Slit

(c)   Detection Screen at 1.0 cm from Center of Aperture Slit

(d)   Detection Screen at 1.5 cm from Center of Aperture Slit

(e)   Detection Screen at 2.0 cm from Center of Aperture Slit

(f)   Detection Screen at 2.5 cm from Center of Aperture Slit

(g)   Detection Screen at 3.0 cm from Center of Aperture Slit

(n)   Detection Screen at 3.5 cm from Center of Aperture Slit

(.   Detection Screen at 4.0 cm from Center of Aperture Slit

(j)   Detection Screen at 4.5 cm from Center of Aperture Slit

(k)   Detection Screen at 5.0 cm from Center of Aperture Slit

(l)   Detection Screen at 5.5 cm from Center of Aperture Slit

(m)   Detection Screen at 12.0 cm from Center of Aperture Slit

(n)   Detection Screen at 23.0 cm from Center of Aperture Slit

(o)   Detection Screen at 30.0 cm from Center of Aperture Slit

(p)   Detection Screen at 1/4 lambda from Center of Aperture Slit

Screen at slit center, 1.96GHz

(a)
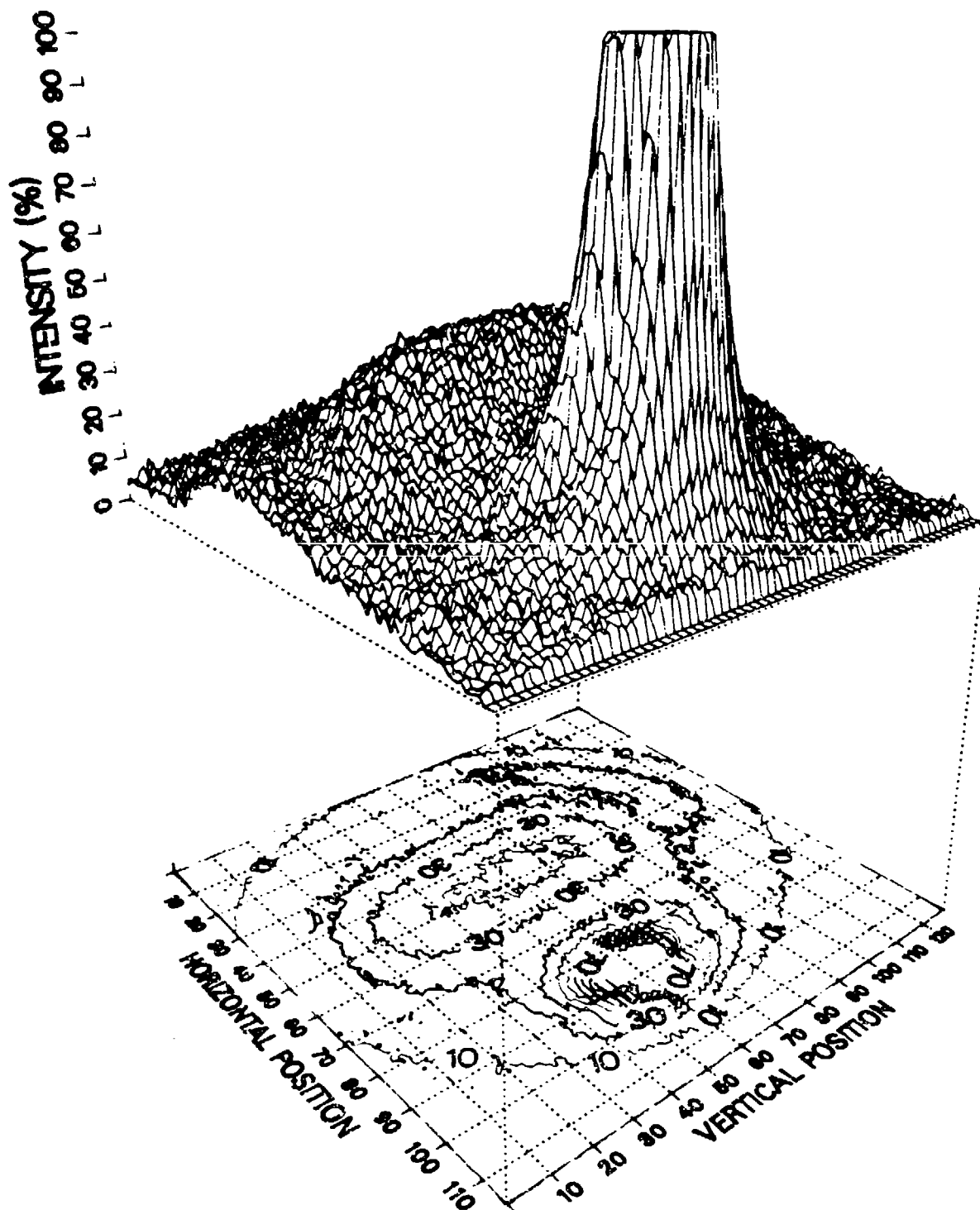
Screen 0.5cm from slit center, 1.96GHz
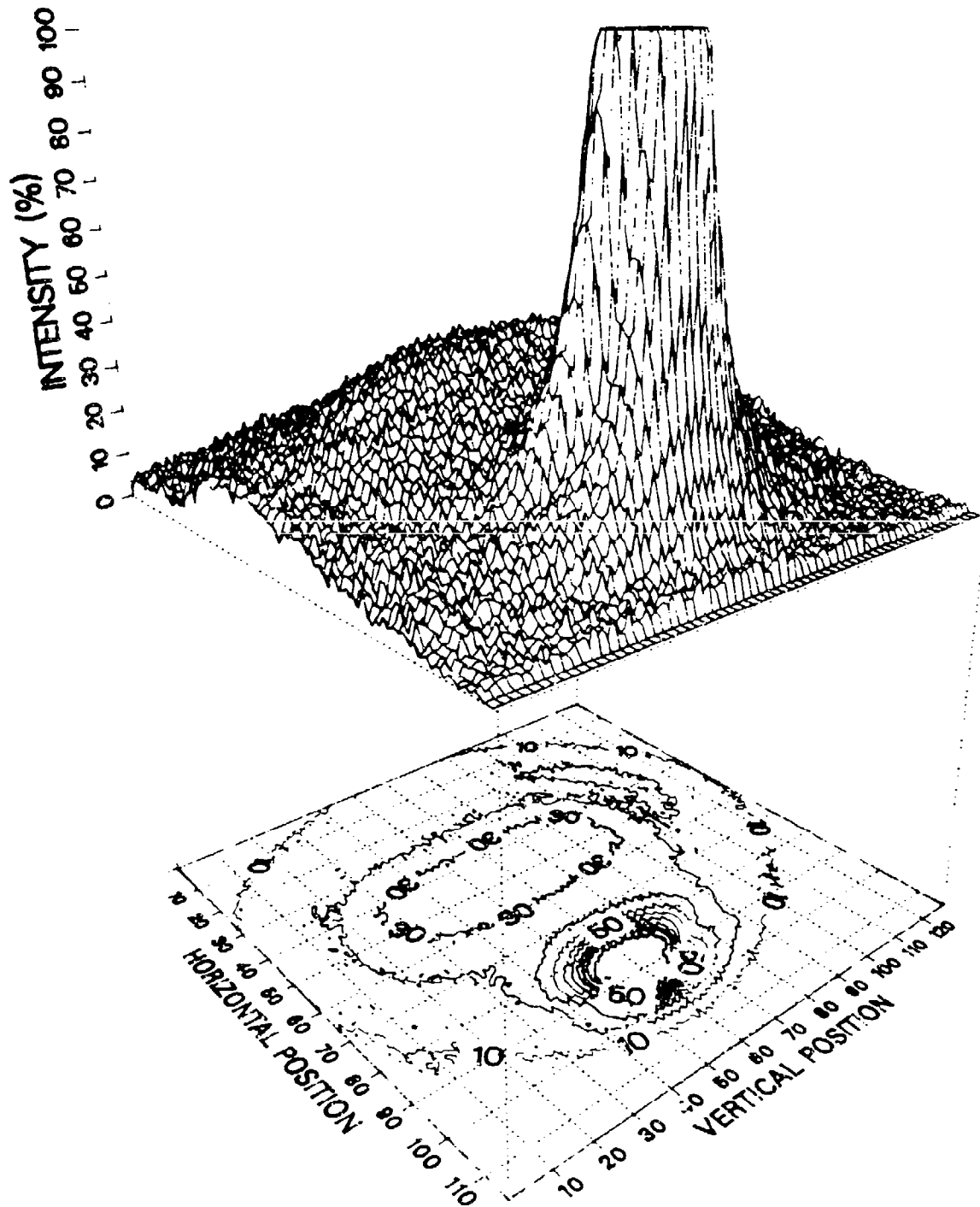
(b)

Screen 1cm from slit center, 1.96GHz

(c)

Screen 1.5cm from slit center, 1.96GHz
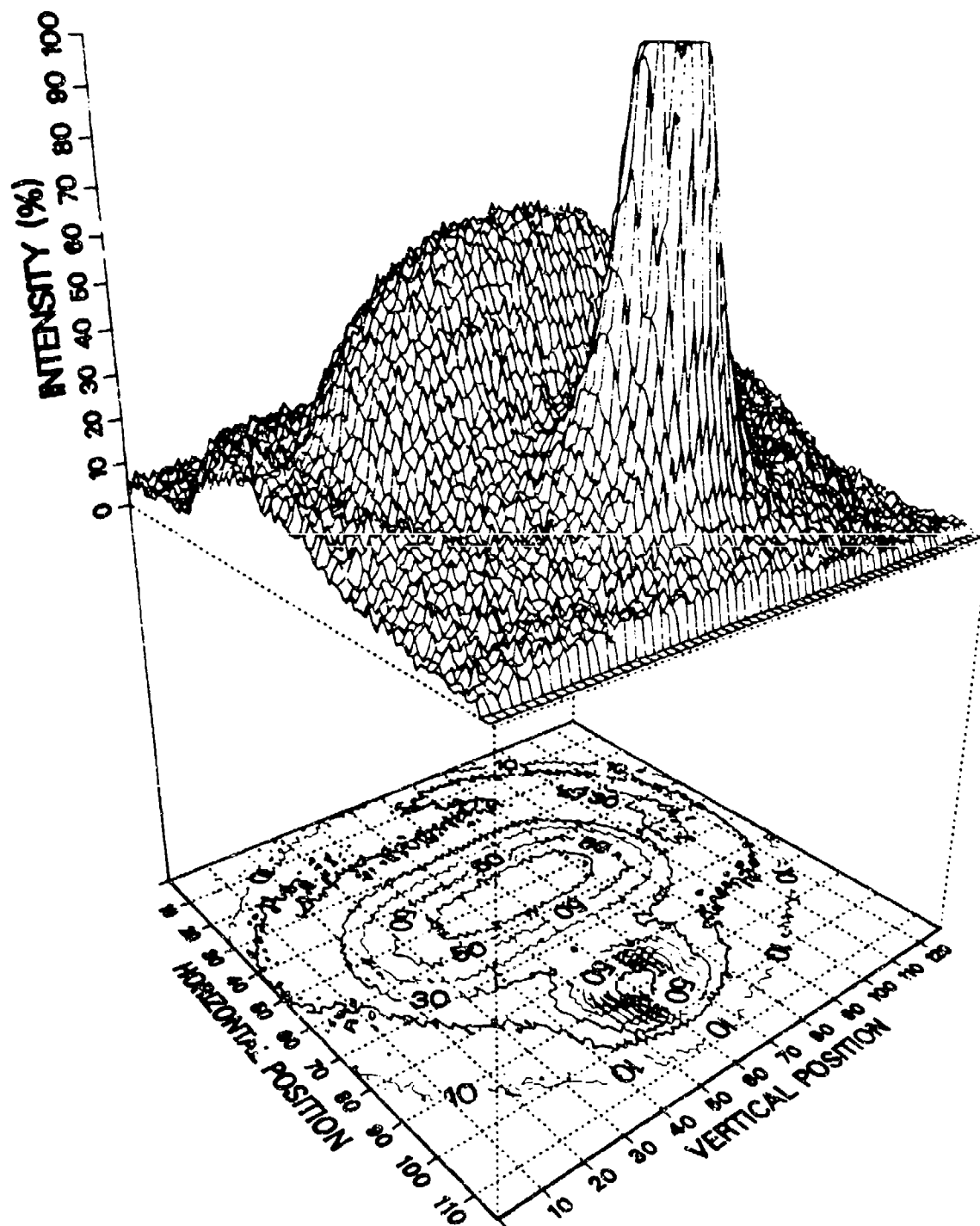
(d)

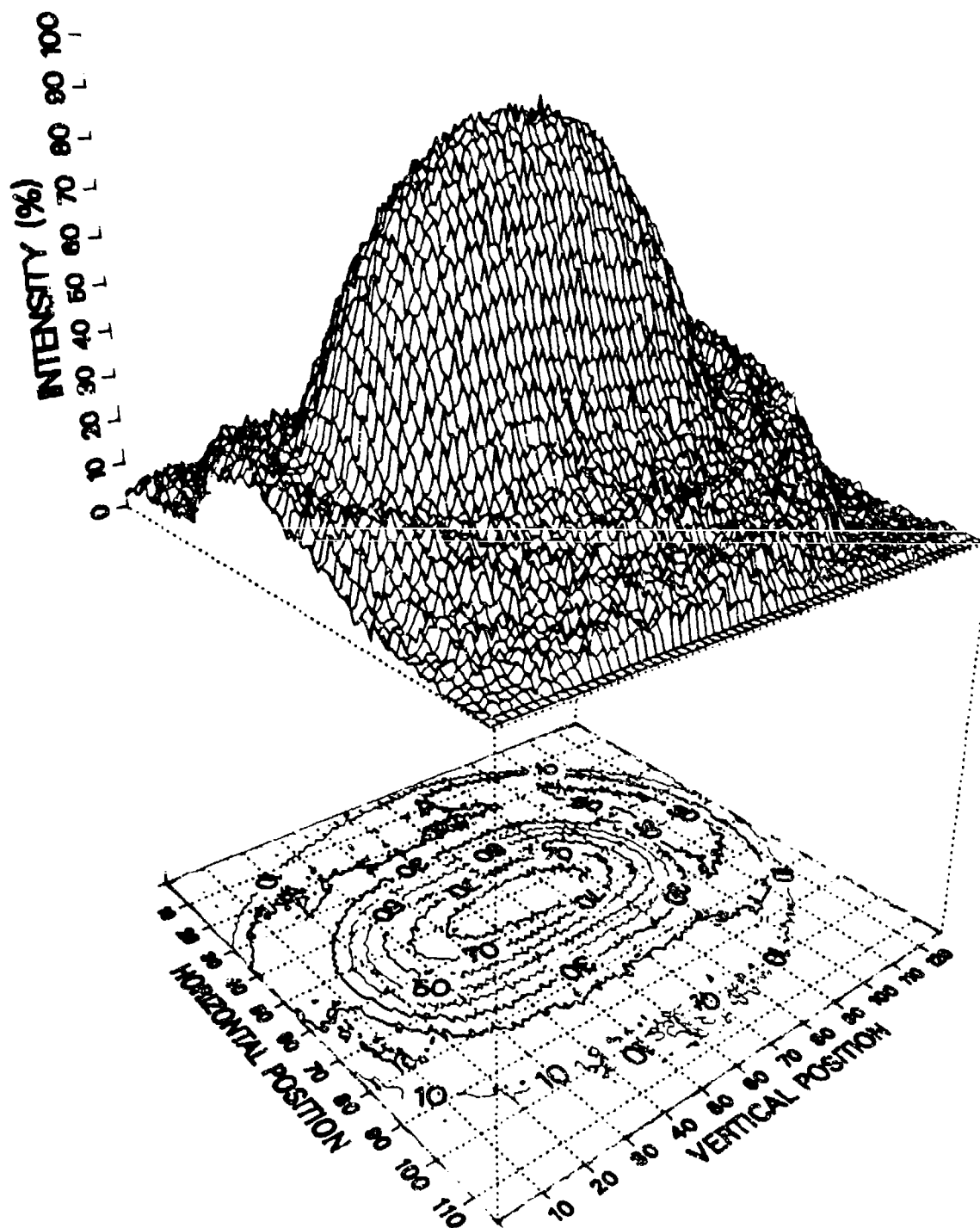# Screen 2cm from slit center, 1.96GHz

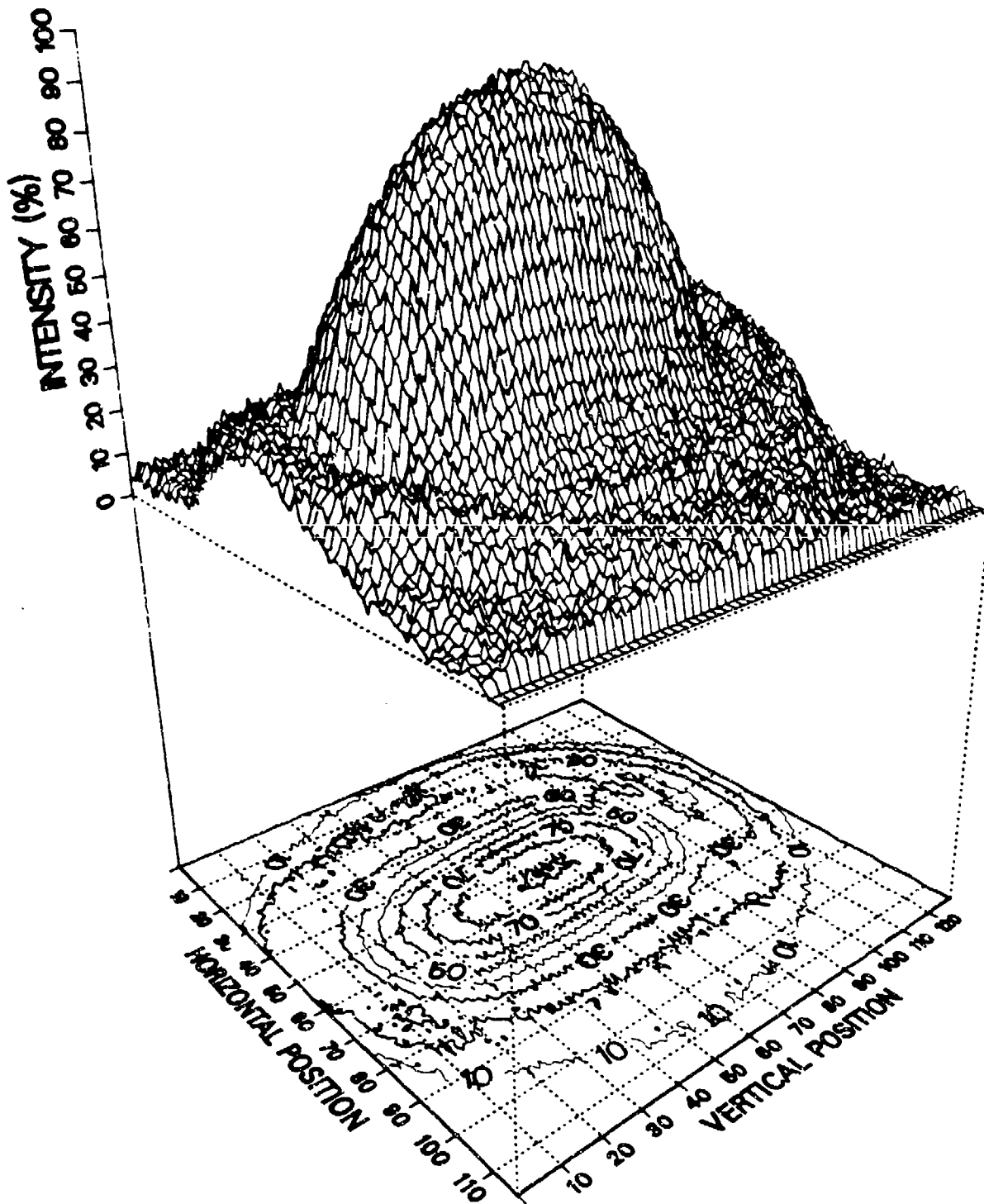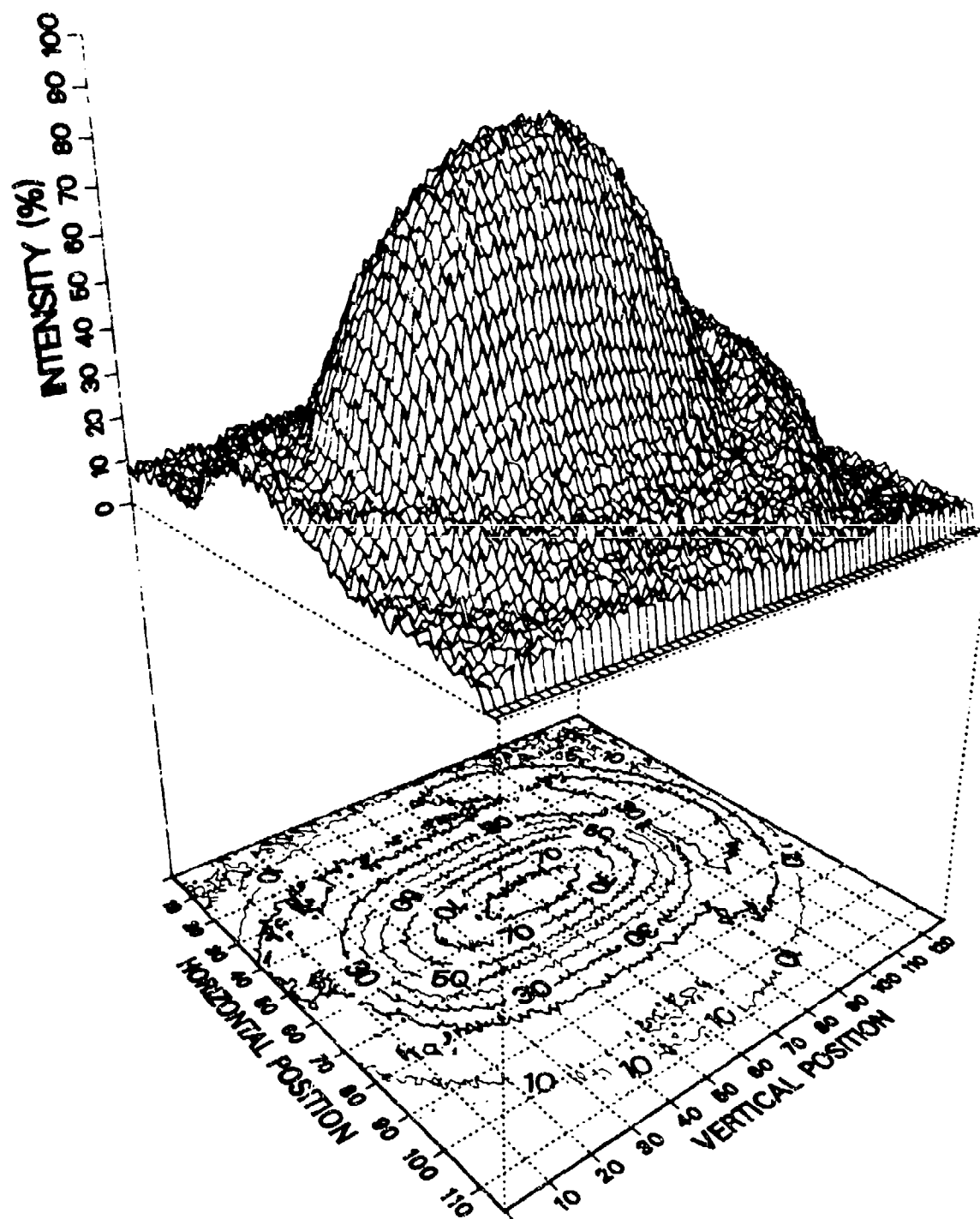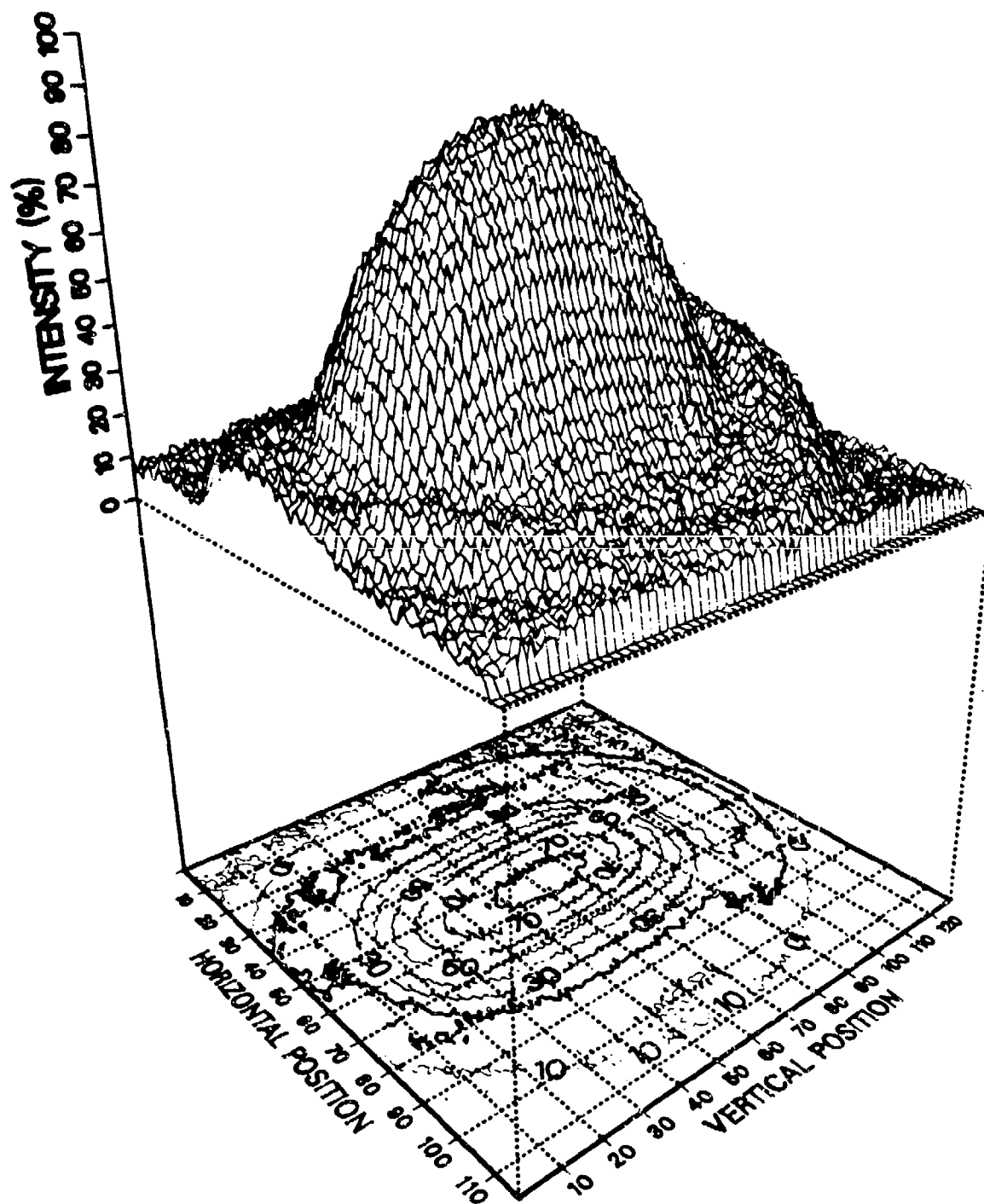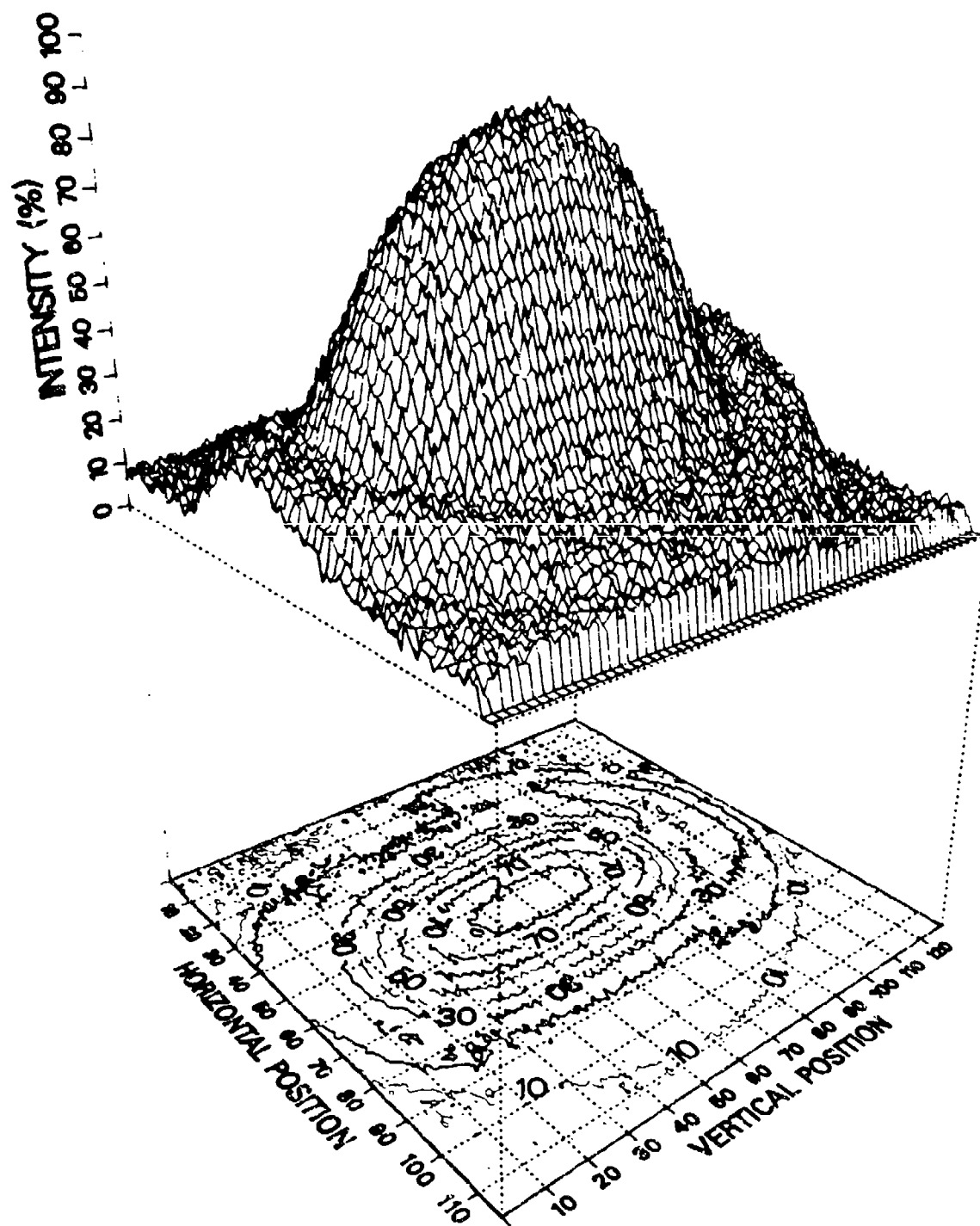(e)

Screen 2.5cm from slit center, 1.96GHz
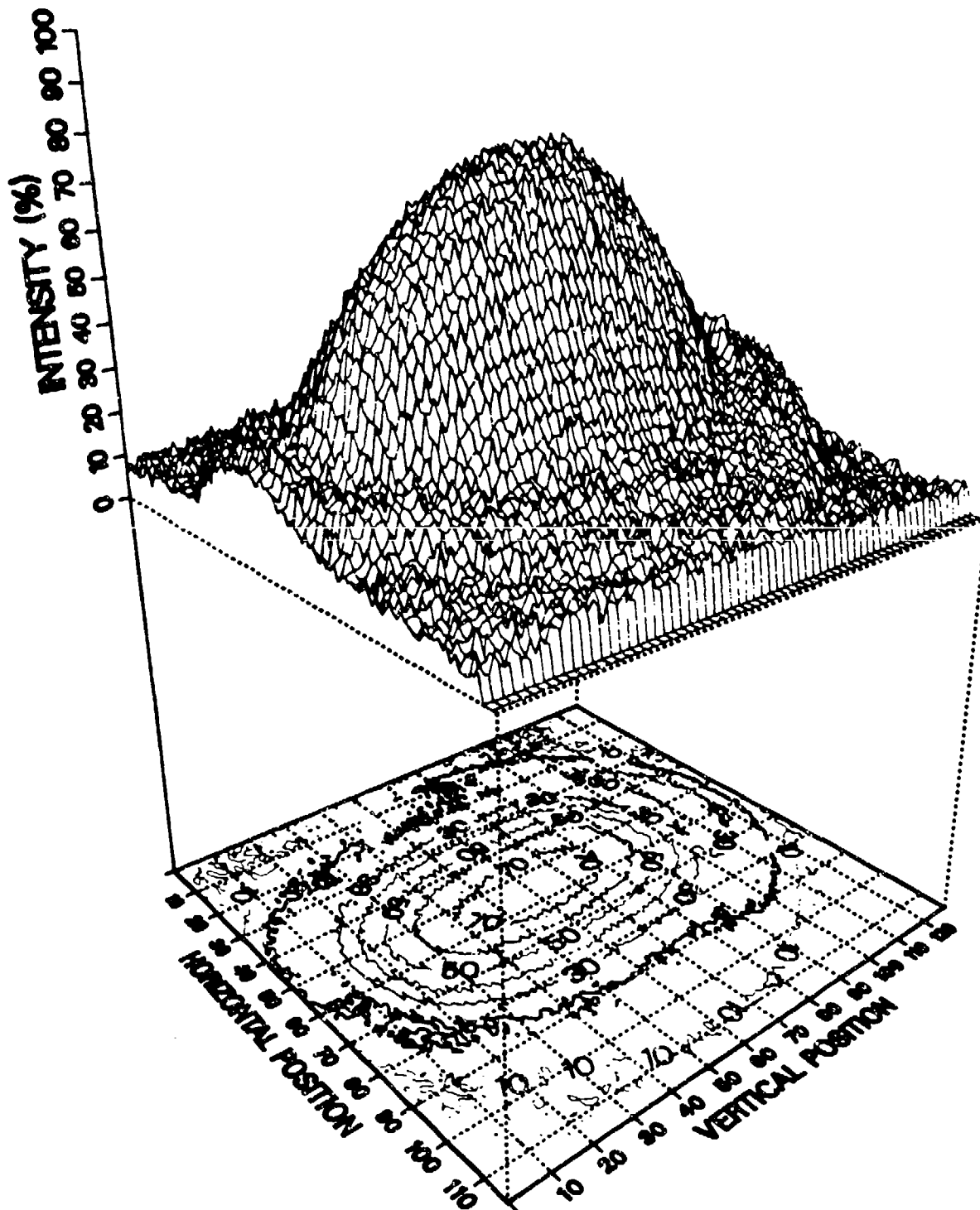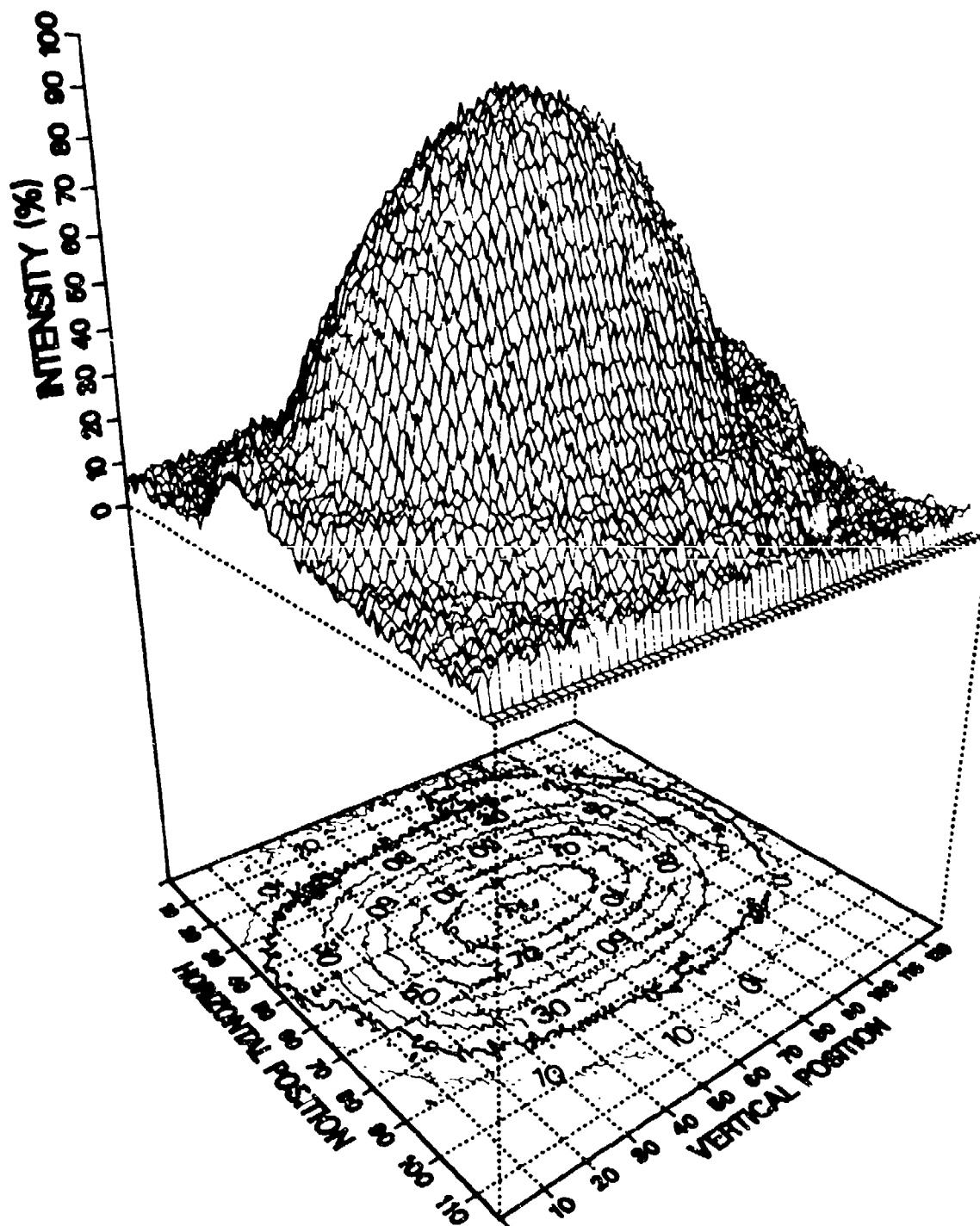
Screen 3cm from slit center, 1.96GHz

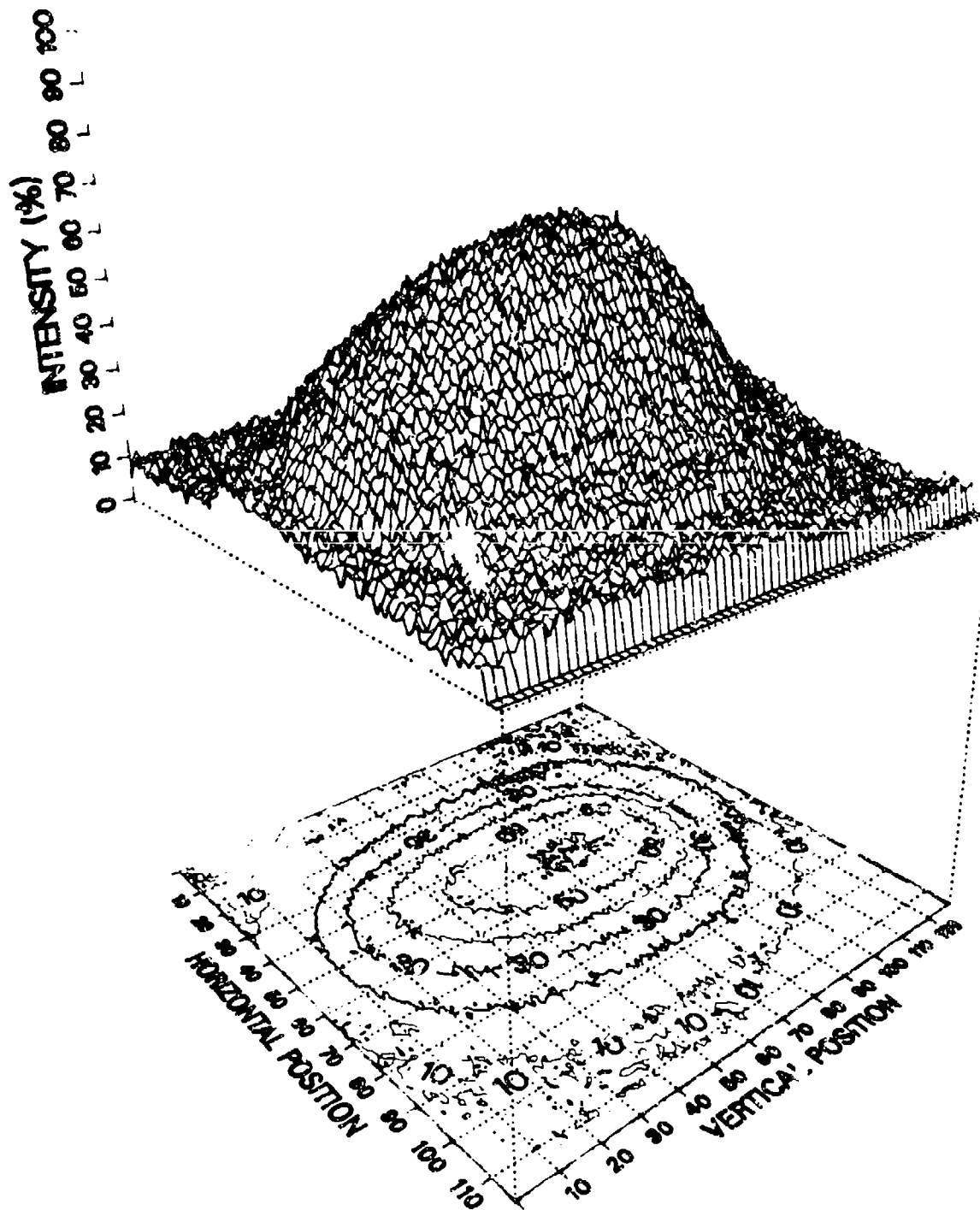(g)

Screen 3.5cm from slit center, 1.96GHz

(h)

Screen 4cm from slit center, 1.96GHz

Screen 4.5cm from slit center, 1.96GHz

(j)

Screen 5cm from slit center, 1.96GHz

(k)

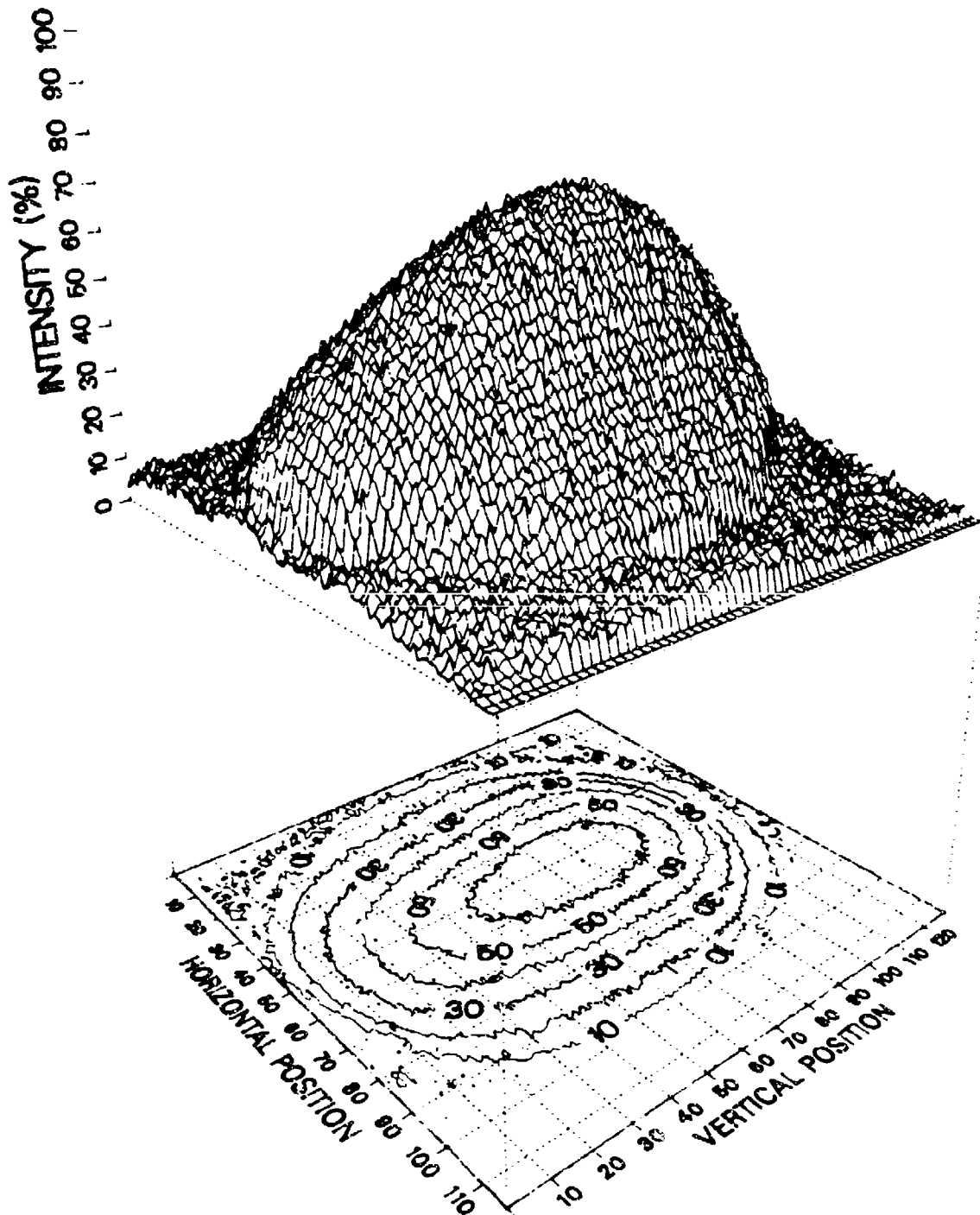# Screen 5.5cm from slit center, 1.96GHz

Screen 12cm from slit center, 1.96GHz

(m)

Screen 23cm from slit center, 1.96GHz

( )

Screen 30cm from slit center, 1.96GHz
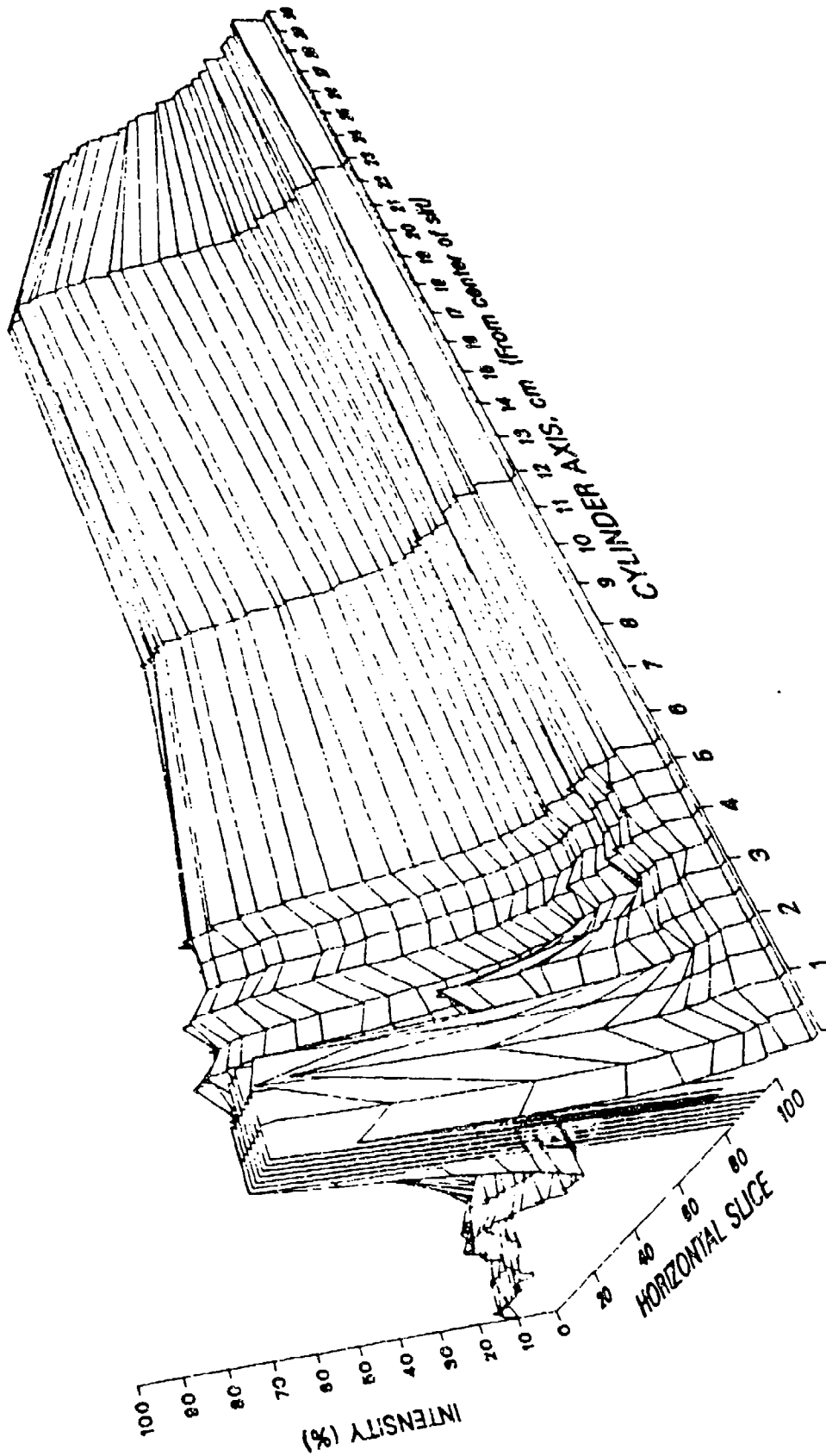

(o)

Screen 1/4 lambda from slit center, 1.96GHz

Figure 13. Longitudinal Relief Map of the Thermogram of the Interior Cylindrical Field at 1.965 GHz Taken Through the Middle of the Cylinder

MISSION

of

Rome Air Development Center

RADC plans and executes research, development, test and selected acquisition programs in support of Command, Control, Communications and Intelligence (C^3I) activities. Technical and engineering support within areas of competence is provided to ESD Program Offices (POs) and other ESD elements to perform effective acquisition of C^3I systems. The areas of technical competence include communications, command and control, battle management information processing, surveillance sensors, intelligence data collection and handling, solid state sciences, electromagnetic and propagation, and electronic reliability/maintainability and compatibility.